REPORT DOCUMENTATION PAGE

Form Approved OMB NO. 0704-0188

1. REPORT DATE (DD-MM-YYYY)	2. REPORT TYPE	3. DATES COVERED (From - To)
07-08-2018	Final Report	3-Feb-2017 - 2-Feb-2018

4. TITLE AND SUBTITLE

Final Report: Increasing the Resolution of Neural Connectivity to Infer Neural Encoding

5a. CONTRACT NUMBER
W911NF-17-1-0093

5b. GRANT NUMBER

5c. PROGRAM ELEMENT NUMBER

6. AUTHORS

5d. PROJECT NUMBER

5e. TASK NUMBER

5f. WORK UNIT NUMBER

7. PERFORMING ORGANIZATION NAMES AND ADDRESSES

University of California - Santa Barbara
3227 Cheadle Hall
3rd floor, MC 2050
Santa Barbara, CA 93106 -2050

8. PERFORMING ORGANIZATION REPORT NUMBER

9. SPONSORING/MONITORING AGENCY NAME(S) AND ADDRESS (ES)

U.S. Army Research Office
P.O. Box 12211
Research Triangle Park, NC 27709-2211

10. SPONSOR/MONITOR'S ACRONYM(S)
ARO

11. SPONSOR/MONITOR'S REPORT NUMBER(S)
70945-LS-DRP.1

12. DISTRIBUTION AVAILIBILITY STATEMENT

Approved for public release; distribution is unlimited.

13. SUPPLEMENTARY NOTES

The views, opinions and/or findings contained in this report are those of the author(s) and should not contrued as an official Department of the Army position, policy or decision, unless so designated by other documentation.

14. ABSTRACT

15. SUBJECT TERMS

16. SECURITY CLASSIFICATION OF:			17. LIMITATION OF ABSTRACT	15. NUMBER OF PAGES	19a. NAME OF RESPONSIBLE PERSON
a. REPORT	b. ABSTRACT	c. THIS PAGE			Ken Kosik
UU	UU	UU	UU		19b. TELEPHONE NUMBER 805-893-5222

RPPR Final Report
as of 28-Aug-2018

Agency Code:

Proposal Number: 70945LSDRP **Agreement Number: W911NF-17-1-0093**
INVESTIGATOR(S):

Name: Ken Kosik
Email: kosik@lifesci.ucsb.edu
Phone Number: 8058935222
Principal: Y

Organization: **University of California - Santa Barbara**
Address: 3227 Cheadle Hall, Santa Barbara, CA 931062050
Country: USA
DUNS Number: 094878394 EIN: 956006145W

Report Date: 02-May-2018 Date Received: 07-Aug-2018
Final Report for Period Beginning 03-Feb-2017 and Ending 02-Feb-2018
Title: Increasing the Resolution of Neural Connectivity to Infer Neural Encoding
Begin Performance Period: 03-Feb-2017 **End Performance Period:** 02-Feb-2018
Report Term: 0-Other

Submitted By: Ken Kosik Email: kosik@lifesci.ucsb.edu
Phone: (805) 893-5222

STEM Degrees: **STEM Participants:**

Major Goals: 1. Apply the recurrent neural network configuration, long short term memory (LSTM), as a universal learning core that can predict connectivity maps across independent neuronal networks, classify neurological conditions and transmit synthetic memory traces. Recordings from multiple electrodes in intact animals are commonly used to train a generalized linear model (GLM) and the model is validated by how effectively the GLM filters predict a behavior. We have developed a system that allows us to directly test the predictions derived from a trained GLM. We built a Neural Circuit Probe that is positioned above a multi- electrode array (MEA) and is capable of identifying the specific neuron from which an MEA signal arises and deliver a chemical reagent such as TTX to that specific neuron. In this manner, if the GLM predicts an inhibitory connection to another neuron we can directly validate the prediction. This level of neuronal connectivity prediction has not been previously accomplished. However, the GLM has inherent limitations mainly related to the assumptions required in by its computation. Among the most limiting assumptions is the necessity to set the amount of history used for the predictions. The use of Long short-term memory (LSTM) architecture represents a promising and incompletely explored approach for prediction of spikes. By training a deep neural network with many neural traces, the “machine” will learn to recognize the patterns as has been demonstrated for other complex problems such as the board game GO that entail numerous instantiations inaccessible to simple rule-based analyses and storage of all possible configurations. LSTM is particularly well–suited to classify, process and predict time series when, in contrast to the GLM, the time lags between events are very long and of unknown size.

2. Build a patterned neuronal network in which a discrete identified signal from one neuronal ensemble induces bursting and synchronization of a second neuronal ensemble. The input signal serves as a memory trigger analogous to a sensory input and the induced firing considered a memory trace or a perception. We will determine whether these traces will be useful as information packets capable of representing synthetic memories or perceptions in comparison to simulated traces in terms of total information content, energy consumption, efficiency and robustness. Machine performance whether it is a recognition task, or a robotic motor task or a game are all limited by their brittleness or the ability to perform within the very narrow confines of the specific task for which the machine was designed. A synthetic memory or perception or behavior is encoded as a set of waveforms. In an engineered system, distinct waveforms corresponding to a set of physical parameters—acceleration, speed, and force—can convey the kinetic aspect of touch. Neurons spontaneously connect in a manner that generates waveforms used for computational purposes according to a still obscure logic. Neural computation is energy efficient and robust; however, the basis for these properties remains inaccessible in part to due to methodological limitations for measuring these parameters in a living neural system.

Accomplishments: 1. Built a patterned array to detect unidirectional axonal conduction signals. The pattern is a

series of triangles connected from the apex of one to the base of another. Axons tend to pass unidirectionally through the apex. Used diffusion methods to compute control over the neuronal ensemble.
2. Developed automated programs to detect synaptic coupling and propagation signals
3. Built and obtained signals using a “drill press” device from cultures grown on glass and inverted onto an MEA.
5. Validated synaptic coupling with cadmium treatment.
6. Determined genotypic specific effects on axonal conduction and synaptic coupling
7. Computationally predicted inhibitory synapses and validated experimentally.
8. Demonstrated patterns of re-wiring on MEAs after complex stimulation.

Training Opportunities: Three graduate students and two post-doctoral fellows have received training

Results Dissemination: 1. Action potential propagation recorded from single axonal arbors using multielectrode arrays.
Tovar KR, Bridges DC, Wu B, Randall C, Audouard M, Jang J, Hansma PK, Kosik KS.
J Neurophysiol. 2018 Jul 1;120(1):306-320. doi: 10.1152/jn.00659.2017. Epub 2018 Apr 11.
2. MEA Viewer: A high-performance interactive application for visualizing electrophysiological data.
Bridges DC, Tovar KR, Wu B, Hansma PK, Kosik KS.
PLoS One. 2018 Feb 9;13(2):e0192477. doi: 10.1371/journal.pone.0192477. eCollection 2018.
PMID: 29425223
3. In vitro Validation of in silico Identified Inhibitory Interactions: Honglei Liu; Daniel Bridges; Connor Randall; Sara A Solla; Bian Wu; Paul Hansma; Xifeng Yan; Kenneth S Kosik; Kristofer Bouchard
(under review)
4. Non-contact monitoring of cellular network electrophysiology
Tal Sharf, Paul K. Hansma, and Kenneth S. Kosik
(in preparation)

Honors and Awards: Elected as a fellow of the AAAS

Protocol Activity Status:

Technology Transfer: UC 2015-001-3; G&C 30794.657-US-WO; NEURAL CIRCUIT PROBE

PARTICIPANTS:

Participant Type: Staff Scientist (doctoral level)
Participant: Kenneth Tovar
Person Months Worked: 6.00 **Funding Support:**
Project Contribution:
International Collaboration:
International Travel:
National Academy Member: N
Other Collaborators:

Participant Type: Other Professional
Participant: Morgane Audouard
Person Months Worked: 11.00 **Funding Support:**
Project Contribution:
International Collaboration:
International Travel:
National Academy Member: N
Other Collaborators:

Participant Type: Other Professional
Participant: Michel Giroux
Person Months Worked: 1.00 **Funding Support:**
Project Contribution:

International Collaboration:
International Travel:
National Academy Member: N
Other Collaborators:

Participant Type: Postdoctoral (scholar, fellow or other postdoctoral position)
Participant: Jiwon Jang
Person Months Worked: 4.00 **Funding Support:**
Project Contribution:
International Collaboration:
International Travel:
National Academy Member: N
Other Collaborators:

Participant Type: Graduate Student (research assistant)
Participant: Honglei Liu
Person Months Worked: 1.00 **Funding Support:**
Project Contribution:
International Collaboration:
International Travel:
National Academy Member: N
Other Collaborators:

Participant Type: Other Professional
Participant: Linying Lu
Person Months Worked: 8.00 **Funding Support:**
Project Contribution:
International Collaboration:
International Travel:
National Academy Member: N
Other Collaborators:

Participant Type: Graduate Student (research assistant)
Participant: Brian Mitchell
Person Months Worked: 3.00 **Funding Support:**
Project Contribution:
International Collaboration:
International Travel:
National Academy Member: N
Other Collaborators:

Participant Type: Graduate Student (research assistant)
Participant: Joshua Mueller
Person Months Worked: 1.00 **Funding Support:**
Project Contribution:
International Collaboration:
International Travel:
National Academy Member: N
Other Collaborators:

Participant Type: Postdoctoral (scholar, fellow or other postdoctoral position)
Participant: Jennifer Rauch
Person Months Worked: 4.00 **Funding Support:**

Project Contribution:
International Collaboration:
International Travel:
National Academy Member: N
Other Collaborators:

Participant Type: Staff Scientist (doctoral level)
Participant: Xuemei Zhang
Person Months Worked: 4.00 **Funding Support:**
Project Contribution:
International Collaboration:
International Travel:
National Academy Member: N
Other Collaborators:

Participant Type: Staff Scientist (doctoral level)
Participant: Hongjun Zhou
Person Months Worked: 3.00 **Funding Support:**
Project Contribution:
International Collaboration:
International Travel:
National Academy Member: N
Other Collaborators:

Use of a Neural Circuit Probe to Validate in silico Predictions of Inhibitory Connections

Honglei Liu[1], Daniel Bridges[2], Connor Randall[2], Sara A. Solla[3], Bian Wu[4], Paul Hansma[2], Xifeng Yan[1], Kenneth S. Kosik[4*], Kristofer Bouchard[5*],

1 Department of Computer Science, University of California, Santa Barbara, USA
2 Department of Physics, University of California, Santa Barbara, USA
3 Department of Physiology, Northwestern University, Chicago, USA
4 Neuroscience Research Institute, University of California, Santa Barbara, USA
5 Biological Systems and Engineering Division, Lawrence-Berkeley National Laboratory, Berkeley, USA

* kenneth.kosik@lifesci.ucsb.edu, kristofer.bouchard@gmail.com

Abstract

Understanding how neuronal signals propagate in local network is an important step in understanding information processing. As a result, spike trains recorded with Multi-electrode Arrays (MEAs) have been widely used to study behaviors of neural connections. Studying the dynamics of neuronal networks requires the identification of both excitatory and inhibitory connections. The detection of excitatory relationships can robustly be inferred by characterizing the statistical relationships of neural spike trains. However, the identification of inhibitory relationships is more difficult: distinguishing endogenous low firing rates from active inhibition is not obvious. In this paper, we propose an *in silico* interventional procedure that makes predictions about the effect of stimulating or inhibiting single neurons on other neurons, and thereby gives the ability to accurately identify inhibitory causal relationships. To experimentally test these predictions, we have developed a Neural Circuit Probe (NCP) that delivers drugs transiently and reversibly on individually identified neurons to assess their contributions to the neural circuit behavior. With the help of NCP, three inhibitory connections identified by our *in silico* modeling were validated through real interventional experiments. Together, these methods provide a basis for mapping complete neural circuits.

1 Introduction

As proposed by D. O. Hebb [1] a "cell assembly" is a network of neurons that is repeatedly activated in a manner that strengthens excitatory synaptic connections. An assembly of this sort has a spatiotemporal structure inherent in the sequence of activations, and consequently strong internal synaptic strengths, which distinguish them from other groups of neurons. Although assemblies of this sort can be defined in numerous ways, one approach is to identify statistically significant time-varying relationships among simultaneously recorded neurons from the spike trains [2–6]. Obtaining these neural activity measurements requires recording from many neurons in parallel that can be spatially localized and temporally resolved at sub-millisecond time scales [7]. Widely used approaches for recording from multiple neurons such as calcium imaging and voltage sensitive dyes as a proxy for electrical activity or multiple

implanted micro electrodes do not satisfy all these requirements. Novel instrumentation is required to meet the challenge of drawing complete neural circuits.

Dissociated neurons can self-organize, acquire spontaneous activity, and form networks according to molecular synaptogenic drivers that can be visualized and probed with multi-electrode arrays (MEAs). The work presented here utilizes MEAs to record signals sub-millisecond time resolution and precise spatial localization. The Neural Circuit Probe (NCP) uses mobile probes for local chemical delivery to a neural circuit of cultured neurons on a commercial MEA with 120 electrodes. Local drug delivery transiently and reversibly modulates the electrical behavior of individually identified neurons to assess their contributions to the circuit behavior. The dynamics of neuronal networks require both excitatory and inhibitory signals. Excitatory cells alone cannot generate "cell assemblies" because such interconnections would only lead to more excitation. A balance between excitatory and inhibitory neurons ensures the stability of global neuronal firing rates while allowing for sharp increases in local excitability which is necessary for sending messages and modifying network connections [8]. In a neuronal network described in terms of correlations among statistically significant time-varying relationships among the spike trains of simultaneously recorded neurons, the detection of excitatory relationships can be inferred based upon correlations between spikes with constant latencies that approximate synaptic transmission [9, 10]. However, the identification of inhibitory relationships is more difficult: distinguishing endogenous low firing rates from active inhibition is not obvious.

In this paper, we demonstrate that tools from statistical inference can predict functionally inhibitory synaptic connections and show how inhibition propagates in a network to affect other neurons. We first fit a Generalized Linear Model (GLM) to spike trains recorded from neurons in hippocampal cultures, and inferred effective interactions between these neurons. We then used the fitted model to perform simulated *in silico* experiments in which we simulated the effect of silencing individual neurons in a network on the activity of other neurons. We tested the predictions from these simulated silencing experiments by performing real experiments in which we applied Tetrodotoxin (TTX) to silence neurons and thereby validated our computational approach toward the detection of inhibitory interactions

2 Methods

2.1 Cell culture

Commercial MEAs (Multi-electrode arrays) were sterilized with UV irradiation (for ¿ 30 minutes), incubated with a poly-D- or poly-L-lysine (0.1 mg/ml) solution for at least one hour, rinsed several times with sterile de-ionized water water and allowed to dry before cell plating. The culture chamber surrounding the MEA was 25 mm in diameter and filled with 1 ml of cell culture media. Cell cultures were prepared in two stages. This was done to allow glia to proliferate and become confluent in the area of the electrodes (1st plating) and for neurons to grow within a substrate of confluent glia (2nd plating). Unless otherwise stated, cells were cultured at 125,000 cells per dish. Mouse hippocampal neurons were used for all experiments described here. All mice were in a C57BL/6 genetic background and male mouse pups were used for all cell cultures. Mouse pups were decapitated at P0 or P1, the brains were removed from the skulls and hippocampi were dissected from the brain [11]. After one week, cultures were treated with 200 uM glutamate to kill any remaining neurons followed by a new batch of cells added at the same density as before. Cultures were grown in a tissue culture incubator (37°C, 5% CO2), in a medium made with Minimum Essential Media with 2 mM Glutamax (Life Technologies), 5% heat-inactivated fetal calf serum (Life

Technologies), 1 ml/L of Mito+ Serum Extender (BD Bioscience) and supplemented with glucose to an added concentration of 21 mM. All animals were treated in accord with University of California and NIH policies on animal care and use.

2.2 Electrophysiology

Most recordings were done in cell culture medium so as to minimally disturb the neurons. In some cases we instead used an extracellular solution containing (in mM) 168 NaCl; 2.4 KCl; 10 HEPES; 10 D-glucose; 1.8 CaCl2; and 0.8 mM MgCl2. Pipette solution contained (in mM): 140 potassium gluconate; 4 CaCl2; 8 NaCl; 2 MgCl2; 10 EGTA; 2 Na2ATP and 0.2 Na2GTP. The pH was adjusted to 7.4 with KOH. The osmolality of external and internal solutions was adjusted to 320 mosmol. Salts were obtained from Sigma-Aldrich or Fluka; TTX was obtained from Ascent Scientific. Recordings were done using MultiChannel Systems MEA 2100 acquisition system. Data were sampled at 20 kHz and post-acquisition bandpass filtered between 200 and 4000 Hz. Recordings were done at 290 to 340 C. All recordings were done on neurons at 7-30 days in vitro (DIV). Data recordings were typically 3.5 to 5 minutes long. Recording duration was typically kept short to minimize the effects of removing MEAs from the incubator. Drug manipulations were done with a custom built instrument that allowed us to apply drug locally.

2.3 Spike sorting

For each MEA recording, we first removed redundancy propagation signals [12] and then did spike sorting [13]. Extracellular signals were band pass filtered using a digital 2nd order Butterworth filter with cutoff frequencies of 0.2 and 4 kHz. Spikes were then detected and sorted using a threshold of 6 times the standard deviation of the median noise level.

The data in Fig 3a were gathered in one recording session and each "unit" corresponds to one spike train after the spike sorting algorithms were applied on the raw data. However, the data in Fig 3d and Fig 3g were gathered in several recording sessions. So, the labels of units could be inconsistent in different recording sessions after the spike sorting algorithms were applied. Hence, to make the data consistent across different recording sessions, for these two datasets, we merged the spike trains from the same electrode as one unit.

2.4 A pipeline to identify and validate putative inhibitory connections

We used a novel pipeline to first identify putative inhibitory connections from spike trains and then validate them with a Neural Circuit Probe (NCP) that we built. Mouse hippocampal neurons were dissociated and plated on a multi-electrode array (MEA). To begin with, as shown in Fig 1a, their spontaneous spiking activity was modeled using a Generalized Linear Model (GLM) in which the outcome is a zero or one (spike or no spike) random variable and single neurons generate spikes according to a Poisson process. The rate of this process was determined by the spikes from other neurons. Parameters of the GLM were fit using a gradient descent algorithm to minimize the negative log likelihood of the recorded spike trains.

We next conducted *in silico* interventional experiments to identity inhibitory connections as shown in Fig 1b. Single neurons were silenced or activated *in silico* and then these data were used to infer predicted effects on connectivity using the fixed parameters from the GLM as determined above. The procedure for running the *in silico* interventional experiment was as follows. First, we selected one neuron as our

interventional target. Throughout the simulation experiment, the state of this neuron was fixed to either 0 (silenced) or 1 (activated). Then, for all the other neurons, we ran the GLM with the inferred parameters to get the probabilities of seeing a spike at the next time point. Each probability represented how likely it was for a neuron to generate a spike at the next time point. Given the probability, we sampled a binary value (0 or 1) from a Bernoulli distribution as the state of the neuron for the next time point, where 0 refers to no spike and 1 means spike. We continued doing this to generate simulated recordings one time point at a time until a desired length T had been reached, where T is the number of time points in our *in silico* interventional recording. To find inhibitory connections, we investigated the generated simulated data to find those neurons that were negatively correlated (Pearson correlation coefficient) with the intervention taken on the target neuron. These neurons were considered as potentially inhibited by the interventional target.

Finally, we conducted real TTX delivery experiments to validate the putative inhibitory connections predicted from the *in silico* interventional experiments as shown in Fig 1c. In these experiments, TTX was delivered using the NCP as a delivery system. The NCP delivered TTX in a manner highly localized to a single electrode and in sufficiently low concentration that its potency dropped below threshold once it diffused beyond a single electrode. The NCP can detect increased impedance as the probe approached the cell and therefore allowed us to deliver TTX as close as possible to the cell without directly contacting the cell. Each TTX delivery resulted in the rapid onset of complete silencing of the neuron to which it was applied. As a result, putative inhibitory connections were validated when we observed activation of an inhibited neuron for a duration that approximated the time of TTX-induced silencing.

2.5 Generalized Linear Model

We used GLM to model the spiking of neurons. Let m denote the number of neurons being recorded and $x_{i,t}$ be the number of spikes of neuron i at time t. We assume $x_{i,t}$ is drawn from a Poisson distribution with rate $\lambda_{i,t}$ which is written as

$$\lambda_{i,t} = \exp\left(b_i + \sum_{j=1}^{m} \sum_{l=minlag}^{maxlag} \theta_{i,j,l} x_{j,t-l}\right). \tag{1}$$

where b_i is a parameter controlling the spontaneous firing rate of neurons i and $\theta_{i,j,t}$ denotes the effective interaction from neuron j to neuron i at time lag l. We assume that the firing rate of neurons i depends on the activities of all neurons in a history window that spans from time $t - maxlag$ to time $t - minlag$, where $minlag$ and $maxlag$ are the minimum and maximum time lags we consider.

Given Eq. 1 for the firing rate of individual neurons, the likelihood for the observation of neuron i at time t, $L_{i,t}$ is

$$L_{i,t} = p(x_{i,t}|\lambda_{i,t}) = \frac{{\lambda_{i,t}}^{x_{i,t}} e^{-\lambda_{i,t}}}{x_{i,t}!}. \tag{2}$$

In spike train data with one millisecond time bin, there are at most one spike at any time point and therefore $x_{i,t}$ takes the value of 0 or 1. Hence, the log-likelihood is

$$\log L_{i,t} = x_{i,t} \log \lambda_{i,t} - \lambda_{i,t}. \tag{3}$$

The log-likelihood for all the observations in a recording with length T is

$$\log L = \sum_{i=1}^{m} \sum_{t=maxlag}^{T} \log L_{i,t}. \tag{4}$$

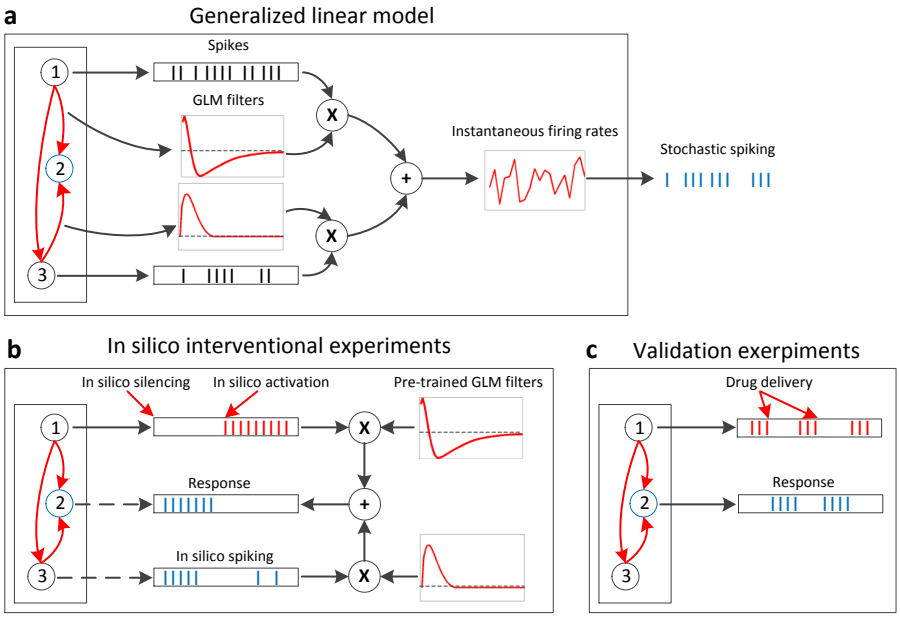

Fig 1. An overview of the procedure that we used to identify and validate direct and indirect inhibitory connections. (a) A Generalized Linear Model (GLM), in which the firing of a neuron is modeled as determined by the spikes from other neurons, was used. Filters of the GLM were inferred from a training recording of spontaneous firings. (b) In silico experiments were conducted by performing simulated interventions on a neuron and generating simulated responses with pre-trained GLM filters. Putative inhibitory connections were then identified by comparing the simulated interventions and responses. (c) Real drug delivery experiments were conducted to validate the putative inhibitory connections.

The model described above includes too many parameters and there is nothing in the model that ensures the inferred parameters to vary smoothly with time, something that isas expected from interactions between pairs of neurons. Furthermore, the model has too many parameters and this might cause problems for robustly inferring them. To ensure the smoothness of the filters, instead of directly using a history window of spikes in the model, following [14], we use their filtered versions that are created by convolving with several cosine bumps. To minimize the number of fitting parameters and prevent overfitting, we add an $L-1$ regularizer to the likelihood. These remedies are described further below.

We first design p cosine basis functions where the l^{th} cosine basis function can be written as:

$$f_l(t) = \frac{1}{2}\{1 + cos[a \ln(t+b) - \Theta_l]\} \tag{5}$$

for all times t such that satisfy

$$-\pi \leq a \ln(t+b) - \Theta_l \leq \pi$$

and

$$f_l(t) = 0$$

outside the interval defined above. The values of a, b and Θ_l are manually chosen. One of the factors to be considered when choosing their values is the locations where the peaks of the bumps occur. During experiments, we used pairwise cross-correlations to determine the locations of the peaks.

In the *naive* GLM without the basis functions, for neuron j, we used a history window of spikes to model its influence on other neurons. Now the raw spikes are convolved with p cosine basis functions to get the filtered versions, of which the l^{th} value is calculated as follows:

$$\tilde{x}_{j,l,t} = \sum_{\Delta=1}^{\tau} f_l(\Delta) x_{j,t-\Delta},$$

where τ is the length of the history window that is covered by the cosine basis functions. Eq. (1) is rewritten as:

$$\lambda_{i,t} = \exp\left(b_i + \sum_{j=1}^{m}\sum_{l=1}^{p} \beta_{i,j,l}\tilde{x}_{j,l,t}\right), \tag{6}$$

where $\beta_{i,j,l}$ is the weight of the l^{th} basis function for the influence from the neuron j to neuron i.

As mentioned above, to prevent overfitting, we added an $L1$ regularization term to penalize non-zero filter parameters. The loss function we want to minimize is rewritten as

$$J = -\sum_{i=1}^{m}\sum_{t=maxlag}^{T} \log L_{i,t} + r\sum_{i=1}^{m}\sum_{j=1}^{m}\sum_{l=1}^{p} |\beta_{i,j,l}|,$$

where r is the regularization constant. The value of r is decided by doing 10-fold cross validation on a spontaneous firing recording of 60 seconds. We used the Area Under the Receiver Operating Characteristic curve (AUC-ROC) as our metric to evaluate the performance of the fitted model to do predictions on future spikes given previous spiking histories.

2.6 *in silico* interventional experiments

To identify inhibitory connections from an ensemble of neurons, one straightforward way is to investigate the GLM filters obtained by fitting the spike trains, as these filters represent the relations of neurons captured by GLM. However, the inhibitory effects among neurons can be rather complex than obvious, and simply using the GLM is usually not enoughsufficient. For example, two of the inhibitory connections we identified in this study were not observable from the their corresponding GLM filters, but became obvious once interventions were applied. Therefore, in this study, we have proposed a method to conduct *in silico* interventional experiments which could discover hidden inhibitory connections by running simulated experiments.

To cold start the simulated experiment, we used a history window of length τ with none spiking states (i.e., all the neurons take the value 0 in a time window of τ). The instantaneous firing rate of neuron i at time t was calculated according to E.q. (6) in Methods section. Therefore, the probabilities of seeing and not seeing a spike are

$$p(x_{i,t} = 1|\lambda_{i,t}) = \lambda_{i,t}e^{-\lambda_{i,t}}$$

and

$$p(x_{i,t} = 0|\lambda_{i,t}) = e^{-\lambda_{i,t}}$$

Because in our setting, there is at most one spike in the one millisecond time bin, $x_{i,t}$ can only take the value of 0 or 1. However, if we run simulated experiments by directly sampling from a Poisson distribution, the value $x_{i,t}$ takes could be arbitrary instead of binary. Hence, we normalize the probability of getting a spike at time point t as

$$\begin{aligned} p(x_{i,t} = 1|\lambda_{i,t}) &= \frac{p(x_{i,t} = 1|\lambda_{i,t})}{p(x_{i,t} = 1|\lambda_{i,t}) + p(x_{i,t} = 0|\lambda_{i,t})} \\ &= \frac{\lambda_{i,t}}{1 + \lambda_{i,t}}, \end{aligned} \tag{7}$$

For neuron i at time point t, we generate the simulated sate by sampling a value from a Bernoulli distribution with the probability of Eq. (7).

During the *in silico* interventional experiments, we selected one neuron as our interventional target and fixed its state to be either 0 (silenced) or 1 (activated). Then, the responses from other neurons were gathered and compared with the intervention taken on the target neuron by calculating their Pearson correlation coefficients. Those neurons that were negatively correlated with the intervention were considered as potentially inhibited by the interventional target. The algorithm is shown in Algorithm 1.

Algorithm 1: Identifying Putative Inhibitory Connections

input : A recording X of spontaneous firing events and a target neuron t
output: Top k neurons that are potentially inhibited by t
Train a GLM model using X
Conduct in silico experiments where neuron t is intervened
for *each neuron* i **do**
  Calculate the Pearson correlation coefficient between simulated recordings of neuron i and neuron t
end
Select top k neurons that have the largest negative Pearson correlation coefficient with neuron t
return top k neuron ids

2.7 Instrumentation for validating putative inhibitory connections

Identification of single cell contributions to a neuronal circuit requires precise access to and control over functionally identified cells. To accomplish this goal we built a neural circuit probe (NCP) consisting of (1) a head unit that accepts various probes, (2) an integrated perfusion chamber plus light ring illumination system, (3) a probe control system with computer interface which implements a simple feedback system for an automated approach, and (4) a commercial MEA (MEA2100, Multi Channel Systems) mounted to a custom X-Y translation stage (Fig 2).

The NCP controller uses proportional and integral feedback control to position the various probes, and can accept a variety of input signals, such as ion current used here. An amplifier is located on the head unit that amplifies the current signal before going to the controller. The NCP software allows the operator to engage and disengage the probe using feedback. It is also used to control the location of the MEA stage beneath the probe, allowing the operator to position the probe above neurons of interest. A pneumatic control system attached to the probe regulates a pressure line for chemical delivery (Fig 2a, Fig 2b). An integrated pressure sensor, connected to the MEA data

acquisition system, measures the duration and magnitude of pressure for temporal alignment with the MEA signal.

Local targeted drug delivery with the NCP can be used to modify their electrical behavior. This was done with small pipettes typically with inner diameters of 1-2 microns. In this example (Fig 2c, Fig 2d) we applied the Na+ channel blocker tetrodotoxin (TTX, 500 nM) to induce a temporary and reversible cessation of activity from that cell. Thus with the NCP we can do targeted drug delivery with high spatial resolution.

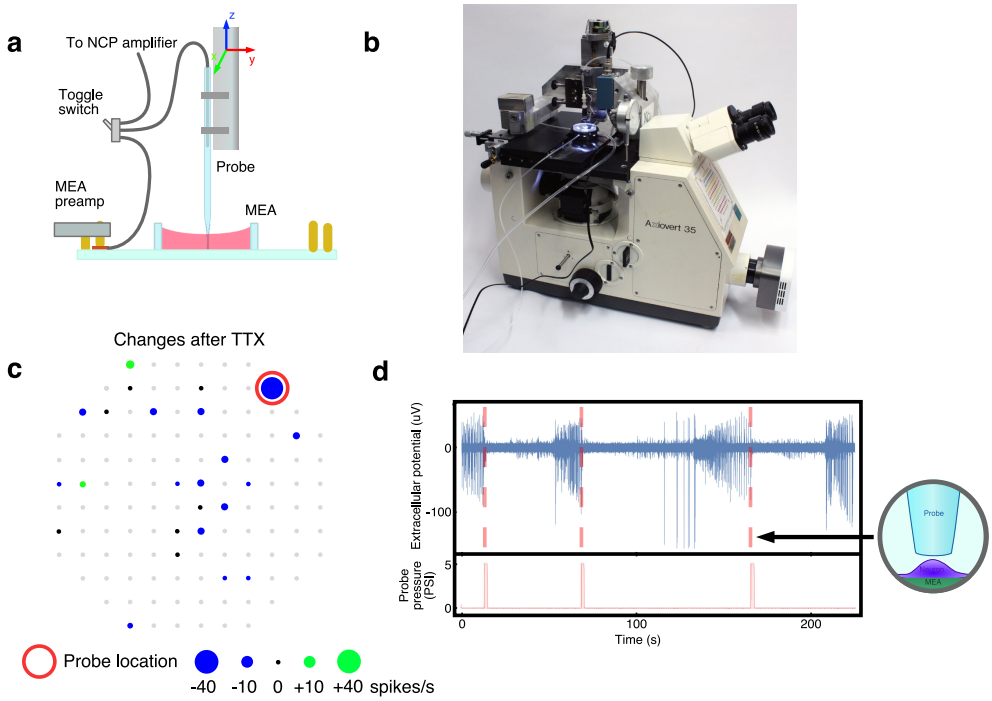

Fig 2. Illustration of the Neural Circuit Probe (NCP) and real drug delivery experiments to validate putative inhibitory connections. (a) Schematic drawing of the key components. The probe is positioned in x and y to center it in the field of view of the microscope. Then the MEA is translated in x and y to bring a target neuron directly under the probe. Finally the probe is automatically lowered, with ion conductance feedback, to just above, but not touching, the neuron. (b) Overview of the NCP situated on an inverted microscope. (c) The changes of firing rates at all electrodes before and after TTX application. Gray dots are electrodes with no spiking activities recorded. Black dots are electrodes with no spiking rate changes. When we blocked spiking at the specific electrode (red circle) it had widespread secondary effects on the firing rates observed at other MEA electrodes. Though the firing rate decreased for many electrodes (blue dots), for two electrodes it increased (green dots). (d) A transient increase of probe pressure delivered TTX (500 nM), which reversibly blocked spiking activity, with high spatial resolution. This process was repeated 3 times.

3 Results

3.1 Identifying Putative Inhibitory Connections

Following the aforementioned procedure, a recording with spontaneous activity from 17 units over a duration of 20 seconds divided into one millisecond time bins was used to

fit the GLM model (Fig 3a). Each unit corresponded to a spike train after spike sorting and removal of the redundancy inherent in propagation signals [12]. Then unit 10 was chosen as the in silico interventional target, i.e. it was fixed in a silent state (no spikes at all times) for 10 seconds and then fixed for 10 seconds in an active state (continuous spiking). Simulations with the fitted GLM identified five units with the highest probability to be inhibited by unit 10 (Fig 3c). The strongest candidate for inhibition by unit 10 was unit 8. Note that the filters from the fitted GLM also suggested that the connection from unit 10 to unit 8 was predominantly inhibitory (Fig 3b).

Additional *in silico* experiments on another cell culture were also conducted to identify putative inhibitory connections by following the aforementioned procedure. For these experiments, we used a 60 second recording of spontaneous firing events (Fig 3d) to fit a GLM. The GLM parameters for the connections from unit 12 to five units are shown in Fig 3e. We calculated the Pearson correlation coefficients between the in silico intervention on unit 12 and simulated responses of every other neuron. The top five negatively correlated units were chosen and investigated (Fig 3f). In another example, we chose unit 23 as the in silico interventional target. Similarly, Fig 3h shows the GLM parameters for the connections from unit 23 to five other units and Fig 3i shows the top five units that were identified as candidates for inhibition by unit 23.

3.2 Validation of Inhibitory Connections

Given putative inhibitory connections identified in the first example (Fig 3c), to validate experimentally that unit 8 was an inhibitory target of unit 10, TTX was delivered four times on unit 10 (Fig 4a) using the neural circuit probe as a delivery tool. The instrument delivered TTX in a manner highly localized to a single electrode and in sufficiently low concentration that its potency dropped below threshold once it diffused beyond a single electrode. Each TTX delivery resulted in the rapid onset of complete silencing of the neuron to which it was applied. Delivery of TTX to the electrode corresponding to unit 10 resulted in the activation of unit 8 and activation of the target neuron for a duration that approximated the time of TTX-induced silencing. These experimental data clearly demonstrated that the top inhibitory connection (from 10 to 8) predicted by our simulated experiment was validated by the actual TTX delivery experiment.

In the second example, 92 was a strong candidate for inhibition by unit 12. To validate this inferred connection experimentally, we delivered TTX to unit 12 and, as predicted, observed an inhibitory effect from unit 12 to unit 92 (Fig 4b). It's also worth mentioning that even though unit 92 is not the top 1 candidate predicted by our *in silico* interventional experiments, it's within the top 5 predictions out of 120 possible units. This shows that the in silico interventional experiments could give accurate predictions of putative inhibitory connections. In the final example, we also delivered TTX to unit 23 and observed rebound of firing on unit 92 (Fig 4c) which was predicted by the *in silico* interventional experiments (Fig 3i).

3.3 Indirect connections

The inhibitory connections identified in this study may not be direct. A unit could be causing inhibitory effects on another unit through a third unit. To study the possibilities of inhibitory connections, we have revisited the three examples of inhibitory connections validated in Fig 4. For each example, we introduced a third unit and convolved the GLM filters of the two connections in a potential inhibitory connection. Fig 5 shows the convolution outputs that exhibited inhibitory effects. To understand the inhibitory effects from unit 10 to unit 8, we show three possible cases where unit 10 could cause an inhibitory effect on unit 8 through a third unit (Fig 6a).

The second example shown in Fig 3 and Fig 4 illustrates an important feature that the in silico experiments offers in describing how signals propagate in the network. In this example the inhibitory effects from 12 to 92 is not obviously manifested in the filters shown in Fig 3e, i.e. the magnitude of the curve representing the connection from 12 to 92 is not as significant as others. However, this inhibitory effect is ranked high according to the negative Pearson correlation score given the simulated experimental results. One explanation for this is the indirect connections among units. It may be the case that unit 12 is not directly inhibiting unit 92, but it could cause an inhibitory effect through other units.

To explore this possibility further, we show three possible indirect inhibitory connections from unit 12 to unit 92 (Fig 6b). Each indirect connection consists of a predominantly excitatory connection and a predominantly inhibitory connection, which could cause a net inhibitory effect. Therefore, it supports the idea that the inhibitory effect from unit 12 to unit 92 were caused by indirect inhibitory connections.

As a final example, Fig 4c shows another inhibitory effect between pairs of neurons, in this case unit 23 to unit 92, as discovered from the *in silico* experiments on the fitted GLM and then validated by experiments. Similarly, we show three indirect inhibitory connections from 23 to 92 (Fig 6c).

4 Discussion

Understanding how neuronal signals propagate in local network is a prerequisite to understanding information processing in those networks. The 'gold standard' way to predict how the activity of one neuron influences another is through intracellular paired recordings along with pharmacologic probes. Using such intracellular recordings, one can establish the presence or absence of direct or indirect connections between pairs of neurons and thus to some degree predict how activity in one neuron affects the others. Inspired by the successes of this technology, we show here how it can be extended to larger networks of neurons using advanced mechatronic positioning of a probe over an array of electrodes with the Neural Circuit Probe. As a demonstration of the potential power of this device, we demonstrated its utility in testing the predictions of *in silico* modeling.

We first fitted a GLM model to spikes recorded from a culture using MEAs, then performed *in silico* experiments in which we silenced one of the units, and identified what other units will change their activity upon this inactivation. We then went back to the culture and silenced the same unit using TTX and observed that the inhibitory effects predicted by the *in silico* experiments showed up when TTX was applied.

The results presented here thus opened the door to using statistical models not only to characterize the statistics of neural spike trains or functional connectivity between neurons, but to make predictions about the response of the network to changes. Although using GLM to study the circuitry of a neuronal network is never going to be as accurate as intracellular recordings, the simplicity of fitting the model to data, and performing in silico experiments with this model, are great advantages that support the idea of using this approach to make educated guesses about the likely outcomes of manipulations to the network, i.e. offering a virtual culture, similar to a previous attempt to use GLMs to build a virtual retina. [15].

In using the GLM in neural data analysis, one typically assumes that a single neuron generates spikes via e.g. a Poisson process. The rate of this process is determined by the spikes from other neurons filtered by interactions that are inferred from data using convex optimization. The inferred model is then used for a variety of purposes that include evaluating the role of correlations in shaping population activity, for example, in the retina [14], the motor cortex [16, 17], the functional connectivity between grid

cells [18], or the relative influence of task related covariates on shaping neural responses in the parietal cortex [19]. Despite the widespread use of the GLM in neural data analyses, a potentially very powerful aspect of this class of models has been left unexplored: the ability of the GLM to make predictions about how a neuronal network responds to interventions. At the microcircuit level, this amounts to identifying meaningful interactions between pairs of neurons and using them to make predictions about how external manipulations of one or more neurons can affect the others. The main reason for the fact that GLMs have not been used for this purposes so far is that, in general, the ground truth about connectivity is not known and, therefore, it is not possible to compare the interactions inferred by GLM with the real ones. The results presented in this paper add a new dimension to how these statistical models can be used in neuroscience by showing that, although the relationship between individual synaptic interactions and those inferred by the GLM may not be known, the inferred connections can still be employed to make specific predictions about the functional connectivity of a neuronal network. Our results thus demonstrate how statistical models can be used to infer neuronal microcircuitry at a detailed level without using more complicated experimental techniques such as multi-unit intracellular recordings.

Supplementary materials

S1 Appendix. Choosing the regularization constant The performance of the GLM was evaluated using a Receiver Operating Characteristic (ROC) curve, which plots true and false positive rates on different axes. The extent to which true positive rates exceed false positive rates is given by the area under the curve (AUC) and was our performance metric to evaluate how well the fitted model could predict future spikes given previous spiking histories. As we can see from Fig 7, the AUC-ROC stops increasing as we increase the regularization constant r to a certain point. We chose r (2.5 in our case) that gave us the best AUC-ROC.

S2 Appendix. Additional functionality of the NCP The NCP also incorporates a mobile electrode to measure extracellular potentials anywhere on the array, providing a higher spatial resolution of the signal versus the standard MEA (Fig 8). The mobile electrode consists of a 20 micron inner diameter micropipette with a 75 micron platinum electrode inserted in the top [20]. A single channel from the commercial MEA preamp is repurposed to measure and record from the mobile electrode. To use the commercial system, the repurposed channel was tapped into using a small piece of conductive film with an insulating layer on the backside, bypassing the electrode on the MEA, and inserting the mobile signal. This technique was necessary to validate the specific neuron that gave rise to the MEA signal of interest.

Acknowledgement

This research was sponsored by the U.S. Army Research Laboratory and Defense Advanced Research Projects Agency under Cooperative Agreement Number W911NF-15-2-0056. The views, opinions, and/or findings contained in this material are those of the authors and should not be interpreted as representing the official views or policies of the Department of Defense or the U.S. Government. Additional support was also provided by the California NanoSystems Institute (CNSI). The funders had no role in the study design, data collection and analysis, decision to publish, or preparation of the manuscript.

References

1. Hebb DO. The organization of behavior: A neuropsychological approach. John Wiley & Sons; 1949.
2. Keat J, Reinagel P, Reid RC, Meister M. Predicting every spike: a model for the responses of visual neurons. Neuron. 2001;30(3):803–817.
3. Pillow JW, Paninski L, Uzzell VJ, Simoncelli EP, Chichilnisky E. Prediction and decoding of retinal ganglion cell responses with a probabilistic spiking model. Journal of Neuroscience. 2005;25(47):11003–11013.
4. Stevenson IH, Rebesco JM, Miller LE, Körding KP. Inferring functional connections between neurons. Current opinion in neurobiology. 2008;18(6):582–588.
5. Stevenson IH, Rebesco JM, Hatsopoulos NG, Haga Z, Miller LE, Kording KP. Bayesian inference of functional connectivity and network structure from spikes. IEEE Transactions on Neural Systems and Rehabilitation Engineering. 2009;17(3):203–213.
6. Pillow JW, Ahmadian Y, Paninski L. Model-based decoding, information estimation, and change-point detection techniques for multineuron spike trains. Neural computation. 2011;23(1):1–45.
7. Gerstein GL, Kirkland KL. Neural assemblies: technical issues, analysis, and modeling. Neural Networks. 2001;14(6):589–598.
8. Jonas P, Buzsaki G. Neural inhibition. Scholarpedia. 2007;2(9):3286.
9. Cohen MR, Kohn A. Measuring and interpreting neuronal correlations. Nature neuroscience. 2011;14(7):811–819.
10. Ostojic S, Brunel N, Hakim V. How connectivity, background activity, and synaptic properties shape the cross-correlation between spike trains. Journal of Neuroscience. 2009;29(33):10234–10253.
11. Tovar KR, Westbrook GL. Amino-terminal ligands prolong NMDA receptor-mediated EPSCs. Journal of Neuroscience. 2012;32(23):8065–8073.
12. Tovar KR, Bridges DC, Wu B, Randall C, Audouard M, Jang J, et al. Recording action potential propagation in single axons using multi-electrode arrays. bioRxiv. 2017; p. 126425.
13. Quiroga RQ, Nadasdy Z, Ben-Shaul Y. Unsupervised spike detection and sorting with wavelets and superparamagnetic clustering. Neural computation. 2004;16(8):1661–1687.
14. Pillow JW, Shlens J, Paninski L, Sher A, Litke AM, Chichilnisky E, et al. Spatio-temporal correlations and visual signalling in a complete neuronal population. Nature. 2008;454(7207):995.
15. Bomash I, Roudi Y, Nirenberg S. A virtual retina for studying population coding. PloS one. 2013;8(1):e53363.
16. Truccolo W, Eden UT, Fellows MR, Donoghue JP, Brown EN. A point process framework for relating neural spiking activity to spiking history, neural ensemble, and extrinsic covariate effects. Journal of neurophysiology. 2005;93(2):1074–1089.

17. Rebesco JM, Stevenson IH, Körding KP, Solla SA, Miller LE. Rewiring neural interactions by micro-stimulation. Frontiers in systems neuroscience. 2010;4.

18. Dunn B, Mørreaunet M, Roudi Y. Correlations and functional connections in a population of grid cells. PLoS computational biology. 2015;11(2):e1004052.

19. Park IM, Meister ML, Huk AC, Pillow JW. Encoding and decoding in parietal cortex during sensorimotor decision-making. Nature neuroscience. 2014;17(10):1395–1403.

20. Claverol-Tinture E, Pine J. Extracellular potentials in low-density dissociated neuronal cultures. Journal of neuroscience methods. 2002;117(1):13–21.

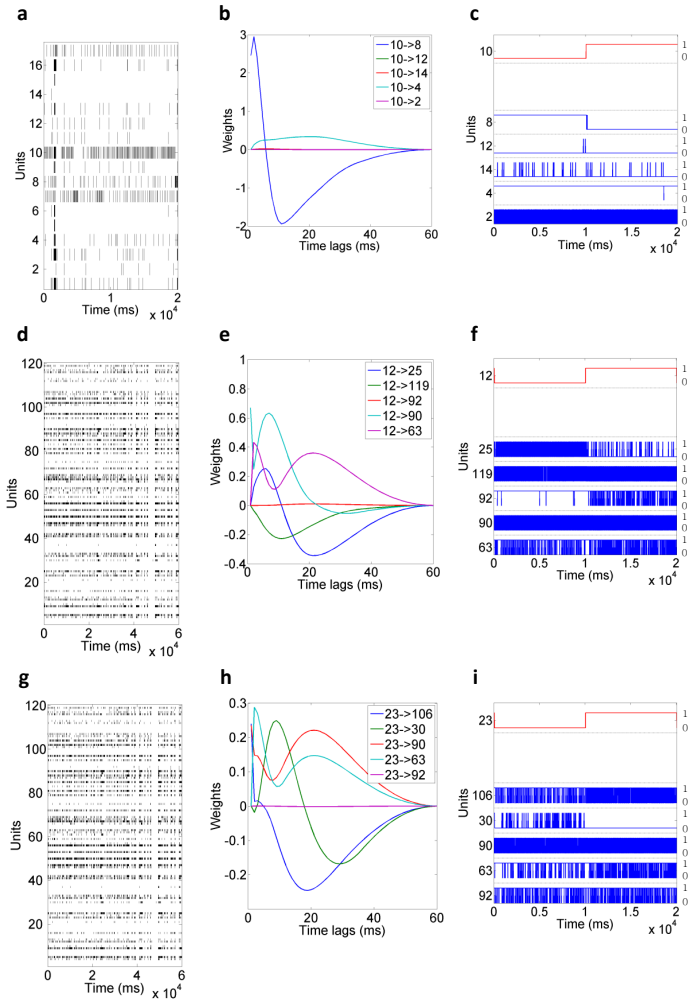

Fig 3. Real data examples of the procedure that we used to identify putative inhibitory connections. (a) A training recording of 17 units for a duration of 20 seconds which were divided into 1 millisecond time bins. The black bars represent spikes. (b) Filters of the GLM inferred from the training recording. Note that at different time lags, the strength of the connection between two units is also different. (c) Simulated data for top 5 units that were negatively correlated with the intervened unit 10. The red and blue lines represent the instantaneous firing rates for the simulated recordings. The labels on the left of the y-axis represent the unit numbers and the labels on the right represent the range of the instantaneous firing rates (0 to 1). Note that when unit 10 was changed from silent state to active state, conversely, unit 8 changed to silent state from active state, which implied a putative inhibitory connection. (d) A training recording of 120 electrodes for a duration of 60 seconds which were divided into 1 millisecond time bins. (e) Filters of the GLM inferred from the training recording. (f) Simulated data for top 5 units that were negatively correlated with the intervened unit 12. (g) A training recording of 120 electrodes for a duration of 60 seconds which were divided into 1 millisecond time bins. (h) Filters of the GLM inferred from the training recording. (i) Simulated data for top 5 units that were negatively correlated with the intervened unit 23.

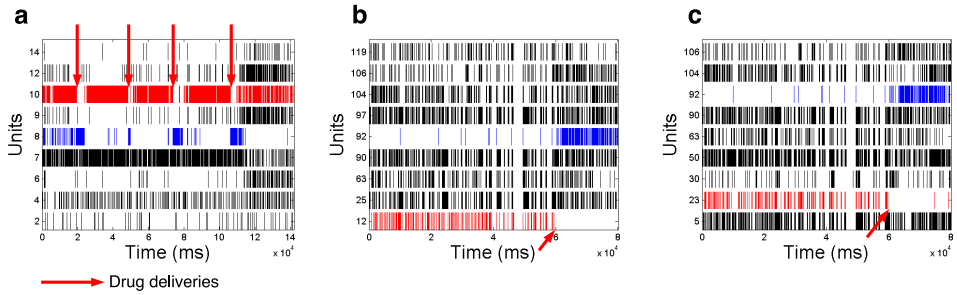

Fig 4. Real TTX experiments to validate putative inhibitory connections. (a) Real TTX experimental recording where unit 10 was silenced 4 times by delivering TTX. Unit 8 rebounded every time unit 10 was silenced, which indicated an inhibitory connection from 10 to 8. (b) Real TTX experimental recording where unit 12 was intervened. (c) Real TTX experimental recording where unit 23 was intervened.

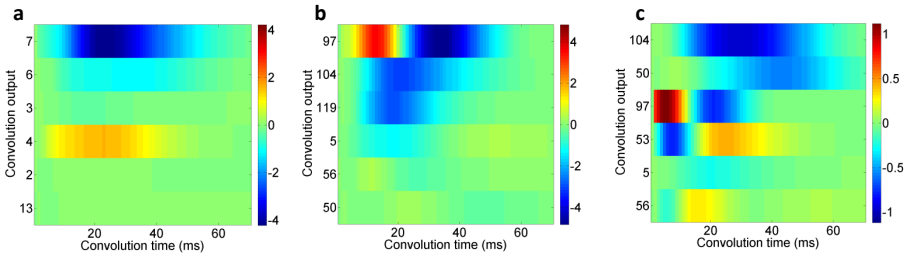

Fig 5. Convolutions of the GLM filters from indirect connections. (a) Convolution of the GLM filters from the connection $10 \to m$ and $m \to 8$, where m (y-axis) is an intermediate unit. The convolutions when m is 10 or 8, which indicates a direct connection, are omitted. (b) Convolution of the GLM filters from the connection $12 \to m$ and $m \to 92$, where m (y-axis) is an intermediate unit. (c) Convolution of the GLM filters from the connection $23 \to m$ and $m \to 92$, where m (y-axis) is an intermediate unit.

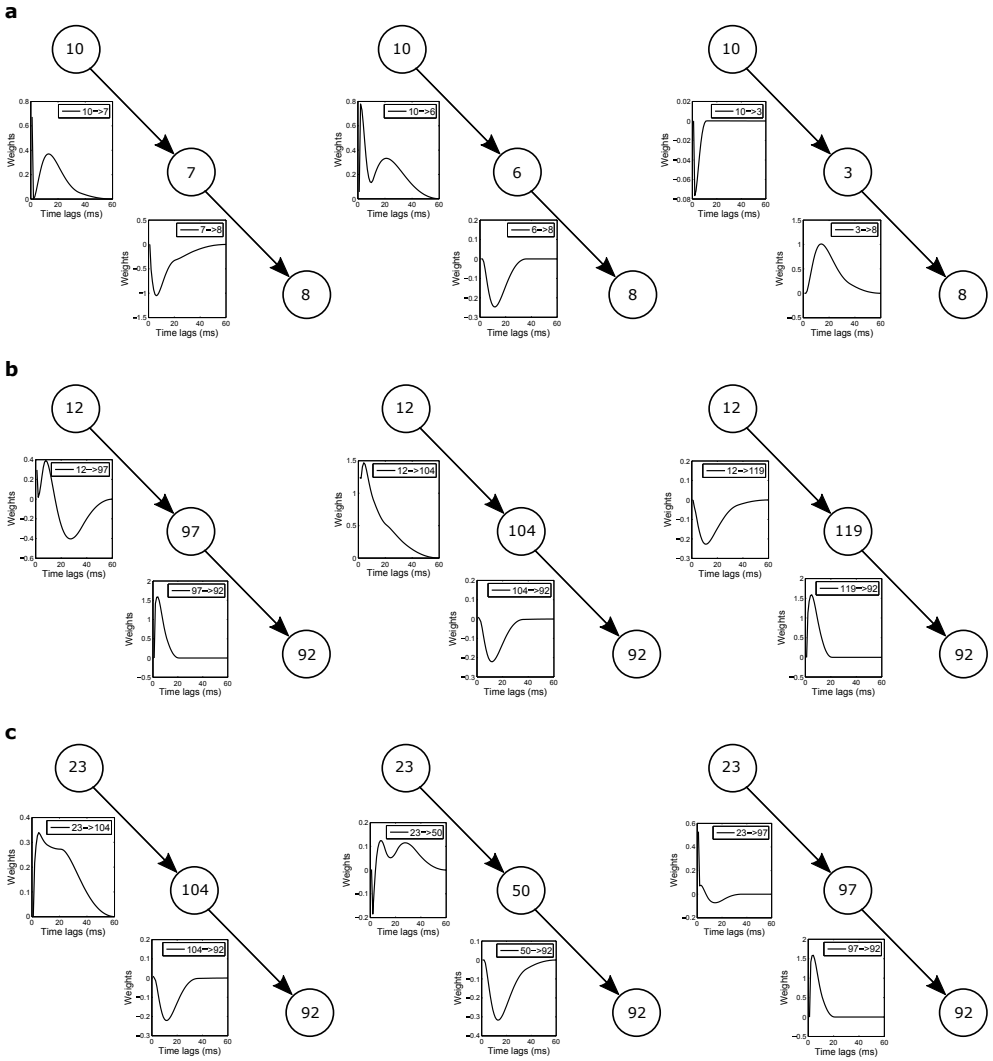

Fig 6. Indirect inhibitory connections. (a) Three possible cases where unit 10 has an inhibitory influence on unit 8 through a third unit. The first case consists of an excitatory connection ($10 \rightarrow 7$) and an inhibitory connection ($7 \rightarrow 8$). The second case consists of an excitatory connection ($10 \rightarrow 6$) and an inhibitory connection ($6 \rightarrow 8$). The third case consists of an inhibitory connection ($10 \rightarrow 3$) and an excitatory connection ($3 \rightarrow 8$). (b) Three possible cases where unit 12 has an inhibitory influence on unit 92 through a third unit. The first case consists of a predominantly inhibitory connection ($12 \rightarrow 97$) and an excitatory connection ($97 \rightarrow 92$). The second case consists of an excitatory connection ($12 \rightarrow 104$) and an inhibitory connection ($104 \rightarrow 92$). The third case consists of an inhibitory connection ($12 \rightarrow 119$) and an excitatory connection ($119 \rightarrow 92$). (c) Three possible cases where unit 23 has an inhibitory influence on unit 92 through a third unit. The first case consists of an excitatory connection ($23 \rightarrow 104$) and an inhibitory connection ($104 \rightarrow 92$). The second case consists of an excitatory connection ($23 \rightarrow 50$) and an inhibitory connection ($50 \rightarrow 92$). The third case consists of a predominantly inhibitory connection ($23 \rightarrow 97$) and an excitatory connection ($97 \rightarrow 92$).

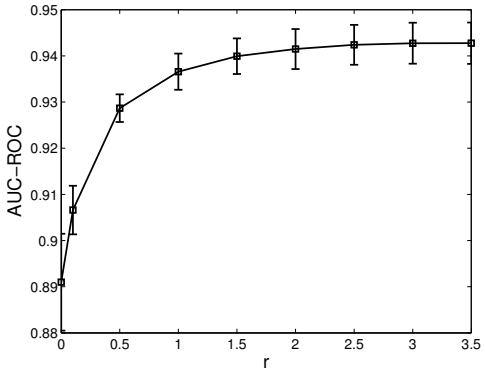

Fig 7. The AUC-ROCs with respect to r. For each value the regularization term has taken, we do a 10-fold cross validation and report the mean and variance.

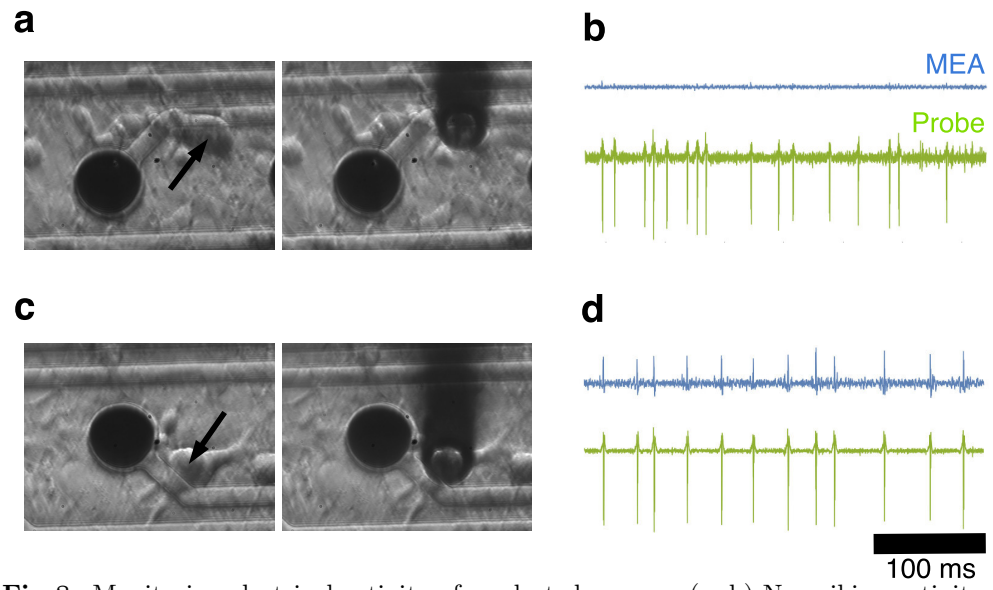

Fig 8. Monitoring electrical activity of a selected neuron. (a, b) No spiking activity was detected on the MEA for the neuron (arrow) closest to the MEA electrode (black circle) whereas a simultaneous recording from the mobile electrode shows robust spiking behavior (compare labelled traces in b). (c, d) The MEA electrode (black circle) closest to the neuron (c, arrow) showed spiking (d, top trace) but when the mobile electrode probe was positioned directly over the cell, the corresponding recording had a higher signal-to-noise ratio.

J Neurophysiol 120: 306–320, 2018.
First published April 11, 2018; doi:10.1152/jn.00659.2017.

Action potential propagation recorded from single axonal arbors using multielectrode arrays

Kenneth R. Tovar,[1] Daniel C. Bridges,[1,3] Bian Wu,[1] Connor Randall,[3] Morgane Audouard,[1,2] Jiwon Jang,[1,2] Paul K. Hansma,[1,3] and Kenneth S. Kosik[1,2]

[1]*Neuroscience Research Institute, University of California, Santa Barbara, California;* [2]*Department of Molecular, Cellular and Developmental Biology, University of California, Santa Barbara, California; and* [3]*Department of Physics, University of California, Santa Barbara, California*

Submitted 5 September 2017; accepted in final form 5 April 2018

Tovar KR, Bridges DC, Wu B, Randall C, Audouard M, Jang J, Hansma PK, Kosik KS. Action potential propagation recorded from single axonal arbors using multielectrode arrays. *J Neurophysiol* 120: 306–320, 2018. First published April 11, 2018; doi:10.1152/jn.00659.2017.—We report the presence of co-occurring extracellular action potentials (eAPs) from cultured mouse hippocampal neurons among groups of planar electrodes on multielectrode arrays (MEAs). The invariant sequences of eAPs among coactive electrode groups, repeated co-occurrences, and short interelectrode latencies are consistent with action potential propagation in unmyelinated axons. Repeated eAP codetection by multiple electrodes was widespread in all our data records. Codetection of eAPs confirms they result from the same neuron and allows these eAPs to be isolated from all other spikes independently of spike sorting algorithms. We averaged co-occurring events and revealed additional electrodes with eAPs that would otherwise be below detection threshold. We used these eAP cohorts to explore the temperature sensitivity of action potential propagation and the relationship between voltage-gated sodium channel density and propagation velocity. The sequence of eAPs among coactive electrodes "fingerprints" neurons giving rise to these events and identifies them within neuronal ensembles. We used this property and the noninvasive nature of extracellular recording to monitor changes in excitability at multiple points in single axonal arbors simultaneously over several hours, demonstrating independence of axonal segments. Over several weeks, we recorded changes in interelectrode propagation latencies and ongoing changes in excitability in different regions of single axonal arbors. Our work illustrates how repeated eAP co-occurrences can be used to extract physiological data from single axons with low-density MEAs. However, repeated eAP co-occurrences lead to oversampling spikes from single neurons and thus can confound traditional spike-train analysis.

NEW & NOTEWORTHY We studied action potential propagation in single axons using low-density multielectrode arrays. We unambiguously identified the neuronal sources of propagating action potentials and recorded extracellular action potentials from several positions within single axonal arbors. We found a surprisingly high density of axonal voltage-gated sodium channels responsible for a high propagation safety factor. Our experiments also demonstrate that excitability in different segments of single axons is regulated independently on timescales from hours to weeks.

Address for reprint requests and other correspondence: K. R. Tovar, Neuroscience Research Institute, UC Santa Barbara, Santa Barbara, CA 93106 (e-mail: ken.tovar@lifesci.ucsb.edu).

action potential; axonal; development; propagation; spike sorting

INTRODUCTION

Axons are the output structures of neurons, broadly integrating and converting subthreshold synaptic potentials to all-or-none action potentials, which are then propagated throughout the axonal arbor. Despite this central role in information transfer, the physiology of mammalian central nervous system (CNS) axons has not been studied in as much detail as more experimentally accessible neuronal structures such as cell bodies or dendrites. Paired axonal recordings have been used to examine the fidelity of action potential propagation (Khaliq and Raman 2005; Meeks et al. 2005; Raastad and Shepherd 2003), as well as the density of voltage-gated sodium channels in axons (Hu and Jonas 2014). However, the small caliber of axons limits their accessibility for routine experimentation using these methods. Voltage-sensitive dyes also have been used to investigate the action potential properties in axons from different classes of cortical neurons (Casale et al. 2015; Zhou et al. 2007). The difficulty of experimentally accessing CNS axons is demonstrated by technically challenging experiments such as these.

Multielectrode arrays (MEAs) are used to record extracellular action potentials (eAPs; also referred to as "spikes") from hundreds of neurons simultaneously (Lewis et al. 2015; Liu et al. 2012). When neurons and glia are cultured on planar MEAs, the electrical behavior of self-organized neural ensembles can be noninvasively monitored over days to weeks (Potter and DeMarse 2001). In these cultures, close apposition of neurons with recording electrodes can produce recordings with high signal-to-noise characteristics, whereas the ease of experimental manipulations in cell culture systems creates opportunities for experiments that are otherwise technically challenging in vivo. Because growth of neuronal processes and electrode orientation are in the same plane, it is reasonable to expect that action potential propagation within single neurons might be detected among multiple electrodes, even in arrays with low electrode density.

We report in this article the widespread co-occurrence of eAPs in cultured mouse hippocampal neurons, with character-

istics expected for detection of action potential propagation, including repeated and invariant sequences of co-occurring spikes at multiple MEA electrodes. Within coactive electrode groups, eAPs occurred with interelectrode latencies that are consistent with propagation velocities reported for unmyelinated axons (Kress and Mennerick 2009). Coactive electrode groups were present in all our data records from cultured mouse hippocampal neurons, and recordings from each unique culture always displayed several distinct and independent coactive electrode groups. Repeated detection of eAPs among electrodes, with submillisecond interelectrode latencies, confirmed that each coactive set of spikes originates from single neurons. The stereotyped sequence and pattern at coactive electrodes unambiguously "fingerprints" and uniquely identifies each neuronal source of these signals. These identified neurons can be thought of as anchor points that can be used to monitor the behavior of single neurons within the larger neuronal network. Averaging the eAP co-occurrences across all MEA electrodes revealed electrodes with subthreshold eAPs, a larger extent of two-dimensional propagation, and, thus, a greater temporal range of interelectrode latencies. We used these propagating eAP signals to examine excitability in single axons during neuronal network development. When we decreased the density of voltage-gated sodium channels, the propagation velocity decreased in a density-dependent manner, but the fidelity of action potential propagation was unaffected, consistent with high axonal sodium channel density. The noninvasive nature of extracellular recording is ideal for monitoring axonal excitability across hours or days. In relatively short time windows, we simultaneously recorded increases and decreases in different segments of single axonal arbors occurring over several hours. Over multiple weeks, our data show that the two-dimensional extent of action potential propagation within single axonal arbors dynamically expands and contracts independently in different parts of the arbor. Recording over these longer time intervals also revealed changes in spike waveforms consistent with changes in action potential duration, changes in the extent and duration of repolarizing conductances, and time-dependent changes in propagation velocity. Our data demonstrate that multisite, noninvasive extracellular recording can be used to study the physiology of single axonal arbors from neurons within a larger neuronal ensemble and to monitor how action potential properties in multiple regions of axonal arbors change over time. These extracellular signals from single neurons are a novel source of empirical ground truth that could be used to test spike sorting algorithms.

METHODS

Cell culture. Cleaned MEAs (120MEA100/30iR-ITO arrays; MultiChannel Systems) were sterilized by UV irradiation (for ~30 min) and then incubated with poly-D- or poly-L-lysine (0.1 mg/ml) for at least 1 h, rinsed several times with sterile deionized water, and either plated immediately after rinsing or allowed to dry before cell plating. The culture chamber surrounding the MEA (19-mm inner diameter) was filled with 1 ml of cell culture medium. Cell cultures were prepared in two stages to allow glia to proliferate and become confluent in the area around the electrodes. The first plating seeds the MEA substrate with proliferating glial cells upon which neurons can grow following the second plating, usually a week later. Cells were plated at 100,000–125,000 cells per dish for the first plating and at 125,000–200,000 cells per dish for the second plating. Mouse hippocampal neurons were used for most of the experiments described. All mice were from a C57BL/6 genetic background, and male mouse pups were used for all cell cultures. For cell culture, mouse pups were decapitated at postnatal *day 0* (P0) or P1, the brains were removed from the skulls, and hippocampi were dissected from the brain. Hippocampi were enzymatically dissociated for 30 min at 37°C and then triturated with flame-polished Pasteur pipettes (Tovar and Westbrook 2012). After the first plating, most neurons did not survive. However, when necessary for timing purposes, cultures were treated with 200 μM glutamate for 30 min at 37°C to kill any remaining neurons. This was done 5–7 days after the first plating. Cultures were grown in a tissue culture incubator (37°C, 5% CO_2) in a medium made with minimum essential medium with 2 mM Glutamax (Life Technologies), 5% heat-inactivated fetal calf serum (Life Technologies), and 1 ml/l Mito$^+$ serum extender (Corning) and supplemented with glucose to an added concentration of 21 mM. Cell culture medium was changed two times per week, and cultures were maintained for as long as 6 wk. We used no antibiotics in our primary neuron cell cultures. All animals were treated in accord with University of California and National Institutes of Health policies on animal care and use.

Solutions, electrophysiology, and analysis. To minimally disturb the neurons and maintain sterility, the recordings described in this work were done in cell culture medium (see above). Recordings were done using a MultiChannel Systems MEA 2100 acquisition system. Data were sampled at 20 kHz and bandpass filtered between 200 and 4,000 Hz after acquisition. Data were recorded on all 120 data channels. We controlled the head-stage temperature with an external temperature controller (MultiChannel Systems TC01). Most recordings reported in this article were done at 30°C, unless otherwise indicated. A small subset of early experiments were done without temperature control. The ambient working temperature of the head stage was ~29°C, setting the minimum temperature at which we could perform experiments. Osmolality of the media was usually ~320 mosmol/kgH_2O. Salts were obtained from Sigma-Aldrich or Fluka; tetrodotoxin (TTX) was obtained from Tocris. For the experiments reported, drugs were introduced directly into the recording chamber in a volume not more than 0.2% of the chamber volume.

All recordings were done on neurons at 5–30 days in vitro (DIV). We only used recordings with signals present on the majority of channels. Recordings were typically 3–5 min long. Recording duration was kept short to minimize the effects of removing MEAs from the incubator and to avoid large changes in CO_2 and pH. All recordings were done with the MEA chambers covered by a CO_2-permeable, water vapor-impermeable membrane (Potter and DeMarse 2001) to minimize the effects of evaporation, maintain cell culture sterility, and decrease degassing of the medium. Membranes were held in place over the recording chamber by a Teflon collar placed over the culture chamber. The temperature of each array was equilibrated to head-stage temperature before data acquisition. This usually required at least 5 min during which we monitored the reequilibration to the specified temperature before recording. Although our recordings were done with covers over the culture reservoir surrounding the MEA, separate control experiments showed that minimizing the recording duration was important because the temperature gradient between the temperature control element, located below the MEA, and the top of the MEA chamber lid promoted evaporation from the small volume of the culture wells and sharply increased the osmolarity of the culture medium (data not shown). When no lid was present, the osmolality of the external solution steadily increased over periods of 45–60 min, accompanied by an increased number of spikes, increased bursting, and decreased interspike intervals. If the cultures were left continuously uncovered long enough (>120 min), spiking decreased and eventually ceased. For experiments requiring temperature changes, head-stage temperature was monitored and each MEA was kept at the new temperature for at least 5 min.

Spike detection and analysis. MultiChannel Systems proprietary files were converted to HDF5 file format with the MCS program Multi

Channel DataManager before all analysis was performed. Extracellular signals were bandpass filtered using a digital second-order Butterworth filter with cutoff frequencies of 0.2 and 4 kHz. Spikes were detected using a threshold of six times the standard deviation of the median noise level (Quiroga et al. 2004). For each eAP detection time, five data points centered on the minimum spike time were fit to a second-order polynomial whose minima was calculated to provide an estimate of the precise spike time. A 3-ms window of the extracellular voltage was then extracted for each spike time. To test the efficiency of spike sorting, eAPs were sorted using a 3-ms spike waveform at each electrode, followed by principle component analysis, with clustering done using the OPTICS algorithm (Prentice et al. 2011). Action potential propagation signals were initially detected by eye with the help of custom spike visualization software and were validated by signal averaging using custom software. Unless otherwise noted, spike-sorted data were not used in our analysis. Analysis was done using Igor (WaveMetrics) and with custom software written in Python and Mathematica (Wolfram). Custom software used in this work is available online (https://github.com/dbridges/mea-tools).

All statistical data are means ± SD. For cases of multiple comparisons, we used analysis of variance followed by the Bonferroni multiple comparison correction. Linear fits to data from manipulation of propagation latency were done using Igor. The percent change in propagation velocity was calculated as

$$\Delta\text{propagation speed } (\%) = 100\left[1/\left(1-m\right)\right] - 100,$$

where m is the average slope for each condition (temperature or TTX concentration).

In some instances, spikes at some coactive electrodes were not reliably detected, even when spikes at other coactive electrodes were detected. This represents either failures of action potential propagation, as might be expected in cases of branch-point failures (Grossman et al. 1979; Soleng et al. 2004) for example, or signal detection failures, such as when eAP amplitude approaches the spike detection threshold. Plotting the probability of eAP detection at constituent propagation signal electrodes as a function of the ratio of eAP amplitude to the spike detection threshold showed that spike detection probability decreased sharply with the spike amplitude-to-threshold ratio. This indicates that occasional failures to detect component propagation signal eAPs at constituent electrodes likely resulted from failures of signal detection rather than failures of action potential propagation. This result is not surprising given the reported high reliability of action potential transmission in hippocampal axons (Cox et al. 2000; Raastad and Shepherd 2003; Radivojevic et al. 2017) but does speak to the level of signal interference from background recording and biological signal noise.

Immunocytochemistry. For immunocytochemistry experiments, neurons and glia were grown on glass coverslips in plastic culture dishes but otherwise prepared and maintained in the same manner as neurons plated on MEAs. Cells were fixed with 4% paraformaldehyde for 15 min at room temperature and washed three times with phosphate-buffered saline (PBS). Cells were then permeabilized with 0.25% Triton X-100 in PBS for 10 min at room temperature and washed three times with PBS. Cells were blocked with BlockingAid (Life Technologies) for 1 h at room temperature and incubated with primary antibodies in the block solution at 4°C overnight. Primary antibodies were diluted at 1:2,000 for the guinea pig anti-vesicular glutamate transporter 1 (anti-VGluT1; catalog no. 135 304; Synaptic Systems) and at 1:1,000 for the rabbit anti-glutamic acid decarboxylase (anti-GAD67; catalog no. 198 013; Synaptic Systems). The cells were washed three times with PBS and incubated with the secondary antibodies in the blocking solutions for 1 h at room temperature. The donkey anti-guinea pig IgG, Alexa Fluor 647 conjugate (catalog no. AP193SA6; EMD Millipore) and donkey anti-rabbit, Alexa Fluor 488 conjugate (catalog no. A-21206; Life Technologies) secondary antibodies were diluted at 1:1,000. Cells were washed three times with PBS and mounted on glass slides with ProLong gold antifade mountant (catalog no. P36934; ThermoFisher Scientific).

Human induced pluripotent stem cell-derived neurons. Neurons were derived from human induced pluripotent stem cells (iPSCs) by NeuroD1 overexpression as described previously (Lalli et al. 2016). Briefly, human iPSCs were passed as single cells with Accutase (StemCell Technologies) and were plated on Matrigel-coated (Corning) plates in mTeSR1 medium (StemCell Technologies) with the RhoA-associated coiled-coil forming kinase (ROCK) inhibitor Y-27632 (StemCell Technologies). The following day, cells were transduced with lentiviral vector NeuroD1-GFP-Puro, driven by a tetracycline-inducible promoter. Two days after transduction, doxycycline (1 μg/ml) was added to the medium to induce the transgene. This stage was designated *day 0*. Transduced cells were selected on *day 1* by adding puromycin (1 μg/ml). On *day 3*, cells were lifted with Accutase and replated on MEAs with mouse glial cells already seeded. From *day 5* to *day 8*, a half-medium change was performed with doxycycline and AraC (1 μM) to kill the proliferating cells in the culture. The induced neurons were maintained and recorded in N2/B27 medium.

RESULTS

Identifying action potential propagation. In every MEA recording from cultures of mouse hippocampal neurons, we noticed repetitively coactive groups of electrodes. Figure 1*A* shows the position of one such group of coactive electrodes indicated within the layout of the MEAs used in our experiments. In our MEAs, the interelectrode distance was 100 μm center to center, and each electrode was 30 μm in diameter. An example of repeated spike co-occurrence at six electrodes is shown in Fig. 1*B*. In this example, during a 180-s-long data record, spikes repeatedly co-occurred at these electrodes more than 1,700 times. An example of repeated eAP co-occurrence from these six electrodes is shown in voltage traces (Fig. 1*B*, arrows). Sequence stereotypy as well as the spike timing latency between coactive electrodes is shown. Data from this record are ordered in time, from the electrode with the earliest occurring spike (F9) to the electrode with last spike in the sequence (D4). During each co-occurrence event, the order of spikes at coactive electrodes was invariant. Each panel in Fig. 1*C* displays the average of 200 eAPs at the indicated electrode, superimposed on 10 individual traces from that electrode. The averaged eAP waveforms resulted from indexing other electrodes to the negative peak of the co-occurring eAPs at the electrode with the earliest occurring eAP (F9). Note that spikes at F9 had the highest amplitude in this group of coactive electrodes. This, in addition to the absence of an initial upward capacitive component of the spike waveform at F9, is consistent with these eAPs originating at or near the axon initial segment (AIS). The characteristic delay between spikes and the sequence stereotypy of these signals during each coactive event are apparent from the averaged events in Fig. 1.

Detection of eAPs at the same neuronal location by two electrodes can occur when electrodes are closely apposed or when the signal-to-noise characteristics are high. The capacitive (positive) component of the eAP in F10 aligns well with the resistive (negative) component of the eAP in F9. The negative peaks of the eAPs at F9 and F10 are consistently offset by roughly 0.3 ms, and the waveforms are quite distinct from each other. These features suggest action potential propagation from F9 to F10 rather than codetection of eAPs at the same cellular region by neighboring electrodes. Moreover, the

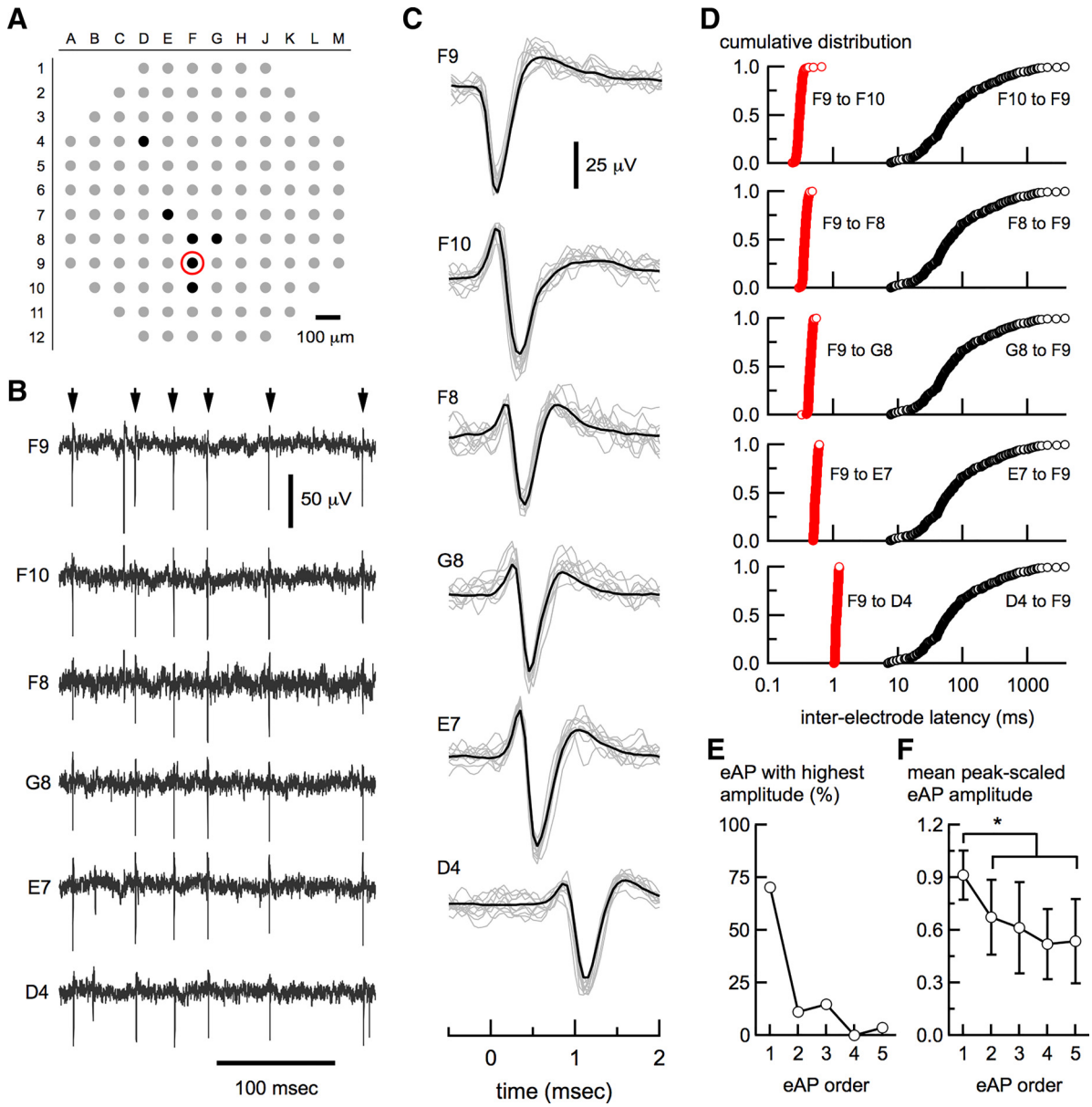

Fig. 1. Coactive extracellular electrodes reveal action potential propagation. *A*: a labeled map of the extracellular electrode configuration. Electrode spacing is 100 μm center to center, and electrodes are 30 μm in diameter. Filled black circles indicate a group of repeatedly coactive electrodes. The earliest spike in this repeating sequence always occurred at F9 (red circle), and the coactive spiking terminated at D4. *B*: extracellular voltage records from the 6 electrodes indicated in *A*. Arrows (*top*) highlight co-occurring spikes among these electrodes. Electrode designations are indicated at *left* of each trace. *C*: spikes from coactive electrodes shown at higher time resolution with averaged spikes (thick black lines) superimposed on 10 individual sweeps (gray lines). Electrode designations are indicated at *top left* above each voltage trace. Note the increasing delay with distance from F9. *D*: cumulative distributions of the latency in spike time between extracellular action potentials (eAPs) at F9 and each of the other electrodes of this coactive sequence (red circles), and the latencies between eAPs at each electrode and the next occurrence of eAPs at F9 (black circles). Note the very short time delays and low variability shown in red. *E*: in 28 groups of coactive electrodes, with 5 component electrodes, the electrode with the highest amplitude was usually the first electrode in the series. *F*: mean amplitudes ($\pm$SD) for spikes in 5-component propagation signals are plotted. Spike amplitudes were normalized to spikes within each co-active electrode group. Normalized amplitudes are higher at the earliest spikes: $^*P < 0.0005$, ANOVA followed by the Bonferroni multiple comparison correction.

combined effect of the large electrode pitch and the fact that extracellular voltage decreases steeply (as $1/r^2$, where r is the radius from a point source; Buzsáki et al. 2012) likely limits simultaneous eAP detection by multiple electrodes in our experiments.

Several features of the eAPs at coactive electrode groups led to the conclusion that these spikes represent action potential propagation, including the invariant sequence of eAP occurrence at constituent electrodes during each coactive event (Fig. 1*C*). Additionally, the interelectrode latencies within each coactive event were consistent with previous reports of propagation velocity in unmyelinated axons. Graphs in Fig. 1*D* each show two cumulative distributions: the interelectrode latencies between the index electrode (F9) and each coactive electrode, and the latency between eAPs at each of the other electrodes (F10, F8, G8, E7, and D4) and the next occurrence of eAPs at F9. The latencies between F9 and each coactive electrode were all in the millisecond-to-submillisecond time domain and highlight the repeated sequence of eAP timing. Note that the latency between the most widely spaced elec-

trodes (F9 and D4) was the longest latency (~1 ms). The progressive latency increase between eAPs at F9 and eAPs at other electrodes is obvious by the rightward shift of their distributions; the low variability of these latency distributions was mirrored by coefficients of variation (CV) ranging from 0.047 to 0.080, consistent with a high-fidelity process like action potential propagation (Meeks et al. 2005). In contrast, the comparatively broad latency distributions between eAPs at other electrodes and the next occurrence at F9 are at least an order of magnitude longer than the other latencies, demonstrating that high spiking frequency among coactive electrodes does not explain the repeated detection of short interelectrode latencies in coactive electrode groups. In 62 unique groups of coactive electrodes, the mean interelectrode interval between consecutive spikes was 0.18 ± 0.15 ms (n = 139). Latencies such as these are too short to be explained by a process such as spiking in pairs of synaptically coupled neurons (3–5 ms; Ivenshitz and Segal 2010).

For the coactive electrodes in this example (Fig. 1), the signal at F9 propagated to D4 (539 μm distant) at ~0.5 m/s, an underestimate of the actual propagation velocity because it assumes a direct path between electrodes. However, this estimate is consistent with reported measurements of action potential propagation in unmyelinated axons from hippocampal neurons (Hu and Jonas 2014; Meeks and Mennerick 2007). Invariant eAPs sequences with submillisecond latencies between coactive electrode groups, along with the low spike timing variability between coactive electrodes, are all consistent with these groups of electrodes detecting action potential propagation in different parts of the same neuron.

The AIS is the site of action potential initiation (Bean 2007; Kole and Stuart 2012) as well as the neuronal region with the highest density of voltage-gated sodium channels (Hu et al. 2009; Kole et al. 2008). The amplitude of the extracellular signal is proportional to the transmembrane current. We thus looked for a relationship between eAP amplitude and the order of occurrence using the relative amplitude of eAPs from 28 unique groups of coactive electrodes in different recordings. Each group contained five coactive electrodes. We first determined the eAP sequence for each group and then peak-scaled the eAP amplitudes to the amplitude of largest average spikes within that group. The eAPs at the first electrode in each sequence had the highest amplitude 70.4% of the time (Fig. 1*E*). Averaging the eAP amplitude at each position to get the mean peak-scaled eAP amplitude for each of the five electrodes of the sequence (Fig. 1*F*) showed the first spike in these sequences, on average, had the highest peak-scaled amplitude (0.91 ± 0.14; $P < 0.00001$, ANOVA and post hoc Bonferroni correction). These results are consistent with detection of high transmembrane current density at or near the AIS. Spike waveforms recorded at the site of action potential initiation lack the capacitive component that results from action potential propagation. The lack of an initial capacitive (positive) peak in the first eAP (Fig. 1*C*) of many sequences in our records is also consistent with eAP detection at or near the AIS. The eAP amplitude decreased by only ~40% at sites distal from the initiating electrode (Fig. 1*F*) contrary to the expectation of a steep gradient in voltage-gated sodium channel density between the AIS and somatodendritic membrane (Cox et al. 2000; Hu et al. 2009; Kole et al. 2008; Lorincz and Nusser 2010). The relatively shallow gradient between the eAPs at the first electrode and eAPs at distal sites (Fig. 1*F*) is consistent with eAPs from coactive groups representing axonal signals. We thus conclude that the repeated eAP co-occurrence and interelectrode latencies reported represent action potential propagation at different segments of neuronal membrane with a high density of voltage-gated sodium channels. We refer to cohorts of eAPs at coactive electrode groups as "propagation signals."

Propagation signals are widespread. Propagation signals were seen in all recordings from mouse hippocampal neurons cultured on confluent layers of glia. In a randomly chosen subset of MEA recordings from these neurons, there were, on average, 7.5 ± 3.4 propagation signals per culture (n = 75 recordings; Fig. 2*A*). In this same data set, there were 4.1 ± 2.4 constituent electrodes per propagation signal (Fig. 2*B*). Therefore, spike redundancy due to propagation signals affected roughly 25% of the MEA electrodes in these recordings (assuming no overlap between electrodes of each propagation signal). The eAP time stamps in a sample of six electrodes from a single MEA recording, showing spike time before and after propagation signals were removed, illustrates the impact of propagation signal redundancy on the raw data record (Fig. 2*C*). In this recording, propagation signals constituted anywhere from 18.9% (H1) to 87.0% (J1) of the total number of spikes from these electrodes. We removed propagation signal eAPs from all but one constituent electrode and decreased the total number of spikes detected in these records by 41.2 ± 19.2% (n = 25 recordings). Electrode density is expected to increase the frequency of detection of propagation signals (Bakkum et al. 2013). We therefore tested how the interelectrode spacing of our arrays (100 μm) contributed to propagation signal detection. This was done with a subset of propagation signals with four electrodes each (the mean number of electrodes per propagation signal). We asked whether we could detect these same signals after retrospectively eliminating every other electrode in these recordings. Even after doubling the interelectrode distance, we still detected propagation signals in 12 of 39 cases, illustrating that larger interelectrode spacing did not eliminate eAP redundancy resulting from detection of action potential propagation. Every recording from cultured mouse neurons contained multiple unique examples of propagation signals. Propagation signals were also present in recordings from human iPSC-derived neurons (data not shown). Our results indicate that redundancy from propagation signal eAPs could significantly compromise spike rate analysis unless taken into account.

The nature of extracellular recording usually precludes assigning the source of an eAP to any particular neuron under study. However, the repeated codetection of propagation signal eAPs among multiple electrodes validates that propagation signal spikes represent action potential propagation in single neurons. The eAP sequence and two-dimensional electrode arrangement creates a unique fingerprint for each signal in the background of spikes from all other sources. We used these characteristics to isolate the firing properties of the individual neurons giving rise to propagation signals, independently of spike sorting routines. The distribution of neuronal firing frequency for 192 propagation signals in records from 39 cultures is plotted in Fig. 2*D*. These firing frequencies in our culture and recording conditions indicate sufficient co-occurring eAPs for the reduction of back-

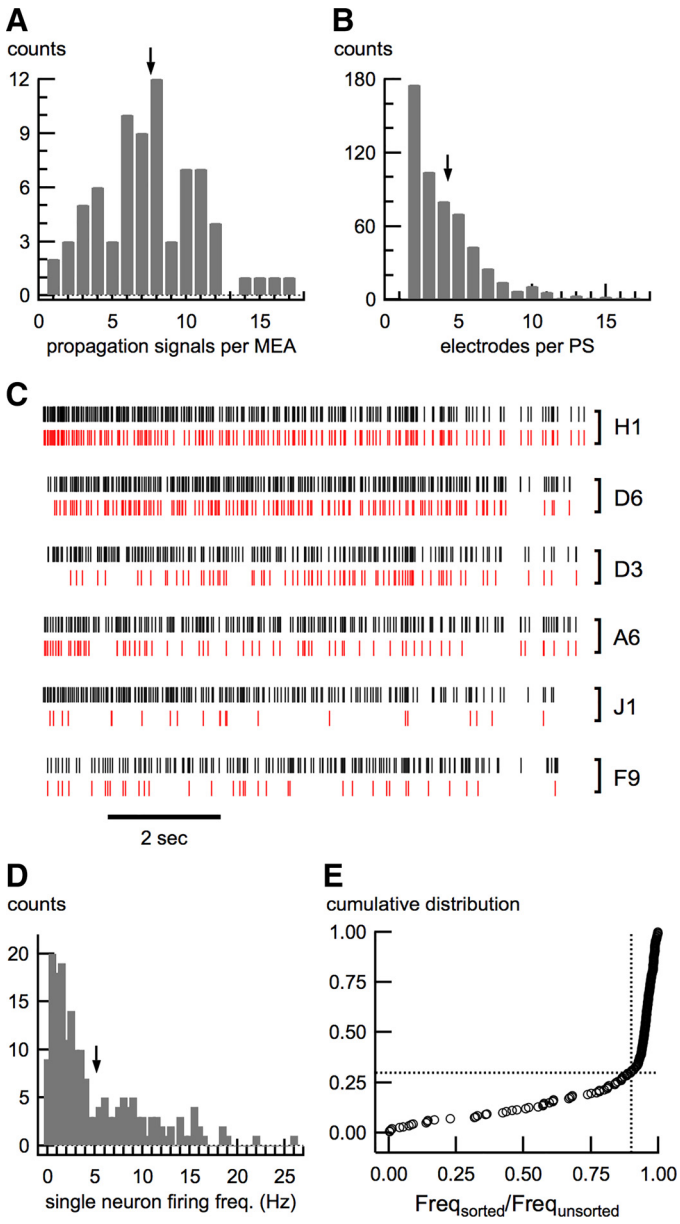

Fig. 2. Widespread occurrence of propagation signals in all multielectrode array (MEA) recordings. *A*: in a distribution of the number of propagation signals per MEA from 75 unique recordings, the average number of propagation signals per MEA was 7.5 ± 3.4. *B*: the distribution of electrodes per propagation signal. For 544 propagation signals, the average number of electrodes per propagation signal was 4.1 ± 2.4. C: results of removing propagation signals on spike trains are graphically demonstrated in 10 s of spike train data from 6 electrodes from the same MEA recording. Spike trains before (black) and after (red) propagation signal removal are displayed. Electrode designations are shown at *right* of each spike train pair. These spike trains are from unsorted data and demonstrate that removal of propagation signals is itself a novel spike sorting step. *D*: the distribution of neuronal firing frequency (mean = 5.03 ± 5.02 Hz, n = 192 propagation signals). *E*: propagation signals were used to assess the performance of a spike sorting routine (OPTICS). This was done by comparing the number of eAP co-occurrences between two electrodes in unsorted and sorted spike trains in the same data records. The efficiency of spike sorting was assessed by using the ratio of the total number of spikes (Freq) in sorted vs. unsorted spike trains for 200 propagation signals. Data are expressed as a cumulative distribution of these ratios. Perfect sorting means that the sorting routine performed as well as propagation signal-based isolation of spikes from single neurons. The vertical dashed line indicates the cutoff where sorting efficiency was 90%. This plot shows that 70% of the 200 propagation signals were at or above 90% sorting efficiency (horizontal dashed line). Arrows in *A*, *B*, and *D* indicate mean values of those distributions. Data are means ± SD.

ground recording noise by signal averaging. These neuronal firing frequencies are consistent with other reports of action potential frequency from hippocampal neurons in vivo (Fenton and Muller 1998; Ranck 1973).

Spike sorting algorithms attempt to cluster eAPs into "units" for subsequent analysis. However, because each extracellular electrode can detect signals from any nearby active neurons, spike sorting routines suffer from a lack of external empirical validation, or "ground truth" (Quiroga 2012). Propagation signals are a novel source of empirical ground truth because the codetection by more than one electrode validates that they result from single neurons. We used propagation signal eAPs to assess the performance of a simple spike sorting routine. We did this by comparing the total number of spikes in eAPs from propagation signals from 200 neurons, in spike-sorted and unsorted data. For each propagation signal eAP we studied, we plotted the ratio of the number of spikes in sorted data to that in unsorted data in a cumulative distribution. A sorting routine that was 100% efficient would result in a ratio of 1, meaning that the sorting routine detected every propagation signal eAP in the unsorted data. In the majority of cases (140/200), our spike sorting routine efficiently sorted at least 90% of the spikes that we detected from unsorted propagation signals (Fig. 2*E*). Thus propagation signals eAPs are a novel source of empirical validation to assess the performance of spike sorting routines. Our data show that propagation signals are widespread in all our cultures and occur with sufficient frequency for signal averaging, which could significantly increase the number of constituent propagation signal electrodes.

Action potential propagation in single neurons at multiple sites. Propagation signal eAPs can be averaged because they result from single neurons. Averaging propagation signal eAPs would decrease the recording noise and reveal electrodes with eAPs otherwise below the spike detection threshold. As shown in Fig. 3*A*, signal averaging reveals electrodes with propagation signal eAPs that would otherwise be below the spike detection threshold. In this example, repeated co-occurrence of eAPs at D9 and F9 was used to isolate this propagation signal. This electrode pair had more than 1,900 co-occurring spikes in 180 s of recording. We averaged 800 of these eAPs at all MEA electrodes in this recording using a 5-ms window centered around the first spike (D9) of the co-occurring pair. Before signal averaging, D9 and F9 were the only electrodes with superthreshold eAPs (Fig. 3*A*); averaging revealed eAPs at 14 additional electrodes, greatly expanding the number of electrodes with eAPs and, importantly, increasing the number of interelectrode latencies. Averaged eAP waveforms were superimposed on 10 sweeps of raw data from a subset of these electrodes (Fig. 3*A*). The eAP detection threshold is shown in each data window, indicating that most signal-averaged eAPs were well below the detection threshold. We superimposed the signal-averaged peak-scaled waveforms of two electrodes with superthreshold spikes and two electrodes with spikes below detection threshold to show the morphological similarity of these eAPs (Fig. 3*B*) and demonstrate the latency between the first and subsequent eAPs. In a subset of 47 unique propagation signals, the average number of electrodes with superthreshold spikes was 3.4 ± 1.6 per propagation signal. Signal averaging each of these propagation signals increased the number of electrodes with eAPs to 18.4 ± 9.2, roughly 15% of the total number of MEA electrodes. We refer to events revealed by

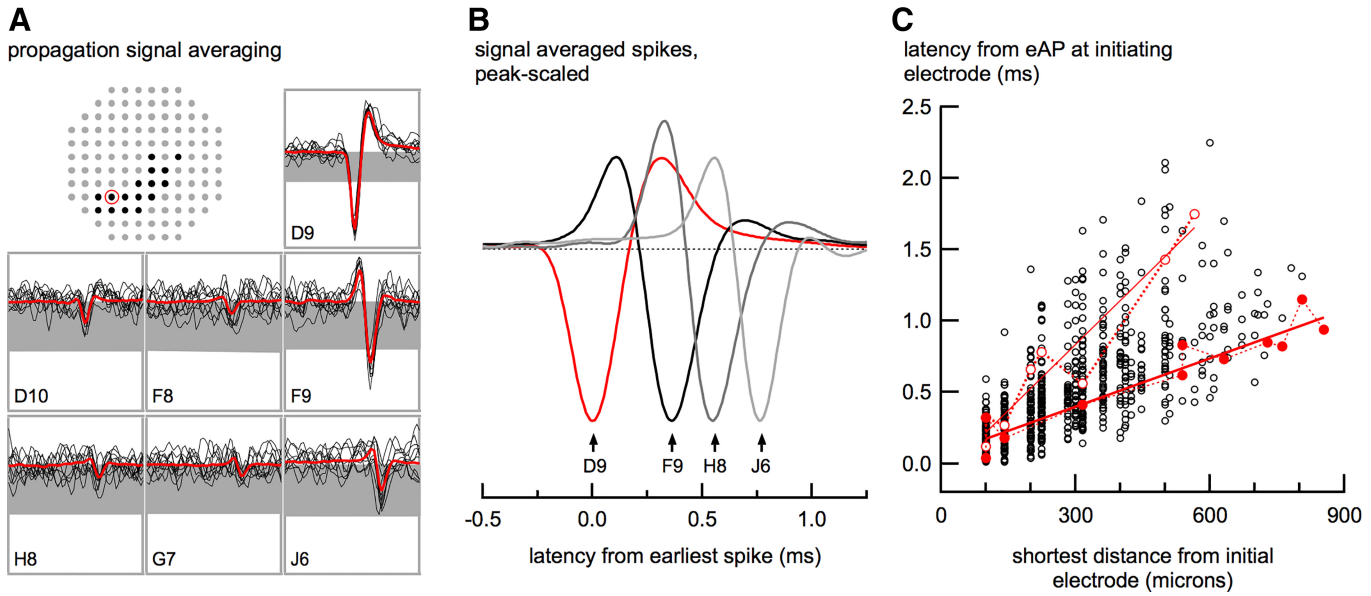

Fig. 3. Signal averaging increases the number of electrodes with propagation signal extracellular action potentials (eAPs). *A*: a map of propagation signal component electrodes, showing sweeps from a subset of those electrodes, centered around the spike at D9. The spike detection threshold for each electrode is indicated by the gray band. Data from each electrode show signal-averaged eAPs (red) superimposed on 10 raw data traces (black). For this signal, eAPs at D9 and F9 electrodes were consistently above their detection thresholds, whereas eAPs at other electrodes were revealed by signal averaging. Vertical axes are the same for all electrodes (50 μV), except for D9 (90 μV). Horizontal axes are the same for all electrodes (3 ms). Electrode layout in this and all subsequent examples is identical to that in Fig. 1*A*. Red circle indicates the electrode where the earliest propagation signal eAP occurred (D9). *B*: subset of super- and subthreshold eAPs from this propagation signal were peak-scaled to the largest negative peak (from electrode D9) and superimposed, highlighting that spikes at distal electrodes tended to occur later in the sequence. Subthreshold eAPs are those that are revealed after signal averaging. *C*: for 50 propagation signals, the latencies between eAPs at initial electrodes and all other signal-averaged eAPs are plotted as a function of shortest distance between electrodes. Data from 2 propagation signals are highlighted with dashed lines connecting red symbols. Linear fits to each are superimposed (solid red lines).

signal averaging as "subthreshold" eAPs. The increased number of electrodes with eAPs resulting from signal averaging increased the temporal range of propagation latencies among the sampling electrodes.

For each propagation signal, we expect that the latency between eAPs at the initial electrode and eAPs at other constituent electrodes tend to would increase as a function of distance. We tested this assumption on propagation signals from 50 neurons by using the cohort of electrodes with signal-averaged eAPs and plotted the latency as a function of shortest distance between electrodes. The plot of latency from the initial eAP to all other propagation signal eAPs (Fig. 3*C*) shows that, as expected, latency tends to increase as a function of distance. Each signal was fit with a linear function; the inverse of the slope of the fits of each of these propagation signals gives a mean propagation velocity of 0.59 ± 0.28 m/s for these neurons (n = 50 propagation signals recorded at 30°C), consistent with previous measurements from unmyelinated axons (Hu and Jonas 2014; Meeks and Mennerick 2007). This estimate represents the lower limit of velocity because it assumes a direct path between electrodes. The increased number of interelectrode latencies per propagation signal that result from signal averaging increases the resolution of measurements that depend on changes in interelectrode latency.

Assessing changes in propagation velocity. Accurately measuring conduction velocity requires knowledge of the propagation path length under study. Acquiring this information routinely is impractical in our system because of the high density of cells (and thus processes) in our neuronal cultures. To bypass the need to know path length and still quantify how experimental manipulations affect propagation velocity, we plotted the change in interelectrode latency as a function of time delay between the index electrode and other constituent electrodes in each propagation signal. We validated our method using the well-known temperature sensitivity of action potential propagation (Chapman 1967; Franz and Iggo 1968; Westerfield et al. 1978).

Figure 4*A*, *top*, shows a map of constituent propagation signal electrodes, including electrodes with super- and subthreshold eAPs. Recordings were done at the indicated temperatures, and eAP latency between the index electrode (B7) and other constituent electrodes is shown in averaged spikes from a subset of these electrodes (Fig. 4*A*, *bottom*). Peak-scaled eAPs at the indicated temperatures show that, as expected, increasing the temperature decreased the eAP latency between the index electrode and each of the other electrodes. We measured changes in action potential propagation induced by temperature by plotting the change in eAP latency as a function of the propagation time at 30°C (Fig. 4*B*, *top*) for every constituent electrode of this propagation signal (Fig. 4*B*, *bottom*). In this example, the slope of the fitted line from the comparison of two back-to-back recordings done at 30°C was flat (m = 0.004 ± 0.004; Fig. 3*E*). In contrast, increasing the temperature decreased the latencies between eAPs at the index electrode (B7) and all other electrodes and increased the slopes in the fitted data. In this example, raising the temperature from 30°C to 33°C increased the slope to 0.147 ± 0.005, reflecting a 17.2% increase in propagation velocity. Increasing the temperature from 30°C to 36°C decreased the interelectrode latency further and increased the slope of the fitted data (0.246 ± 0.007), consistent with the action potential propagation velocity increase of 32.6% at 36°C compared with 30°C.

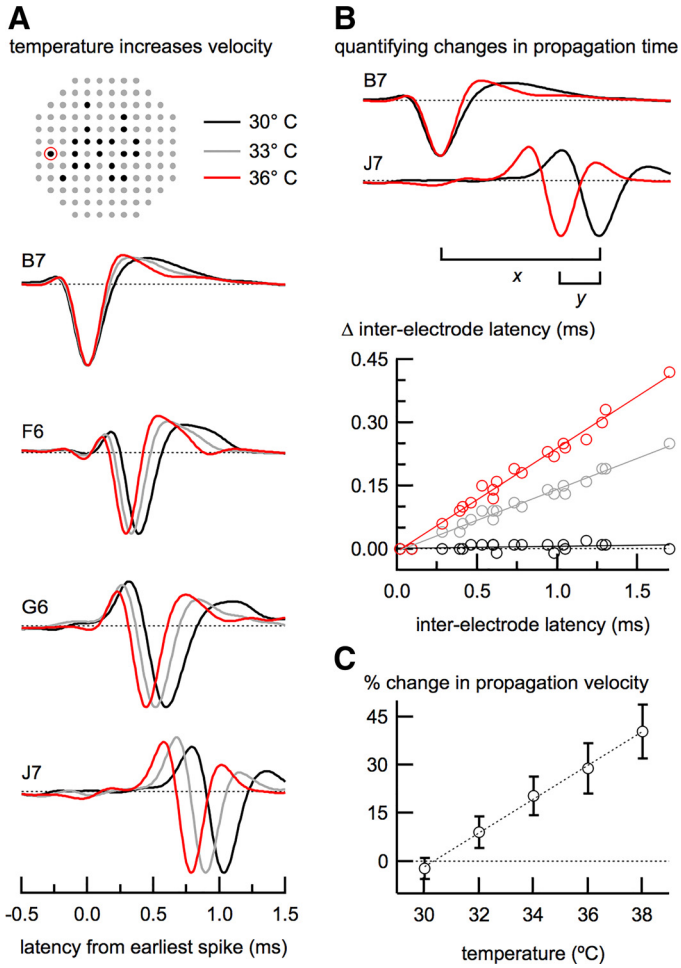

Fig. 4. Quantifying changes in action potential propagation velocity. *A*: a map of electrodes with super- and subthreshold extracellular action potentials (eAPs) for 1 propagation signal (*top*) and a subset of those eAPs recorded at 30, 33 and 36°C (*bottom*). Changes in propagation velocity were indexed to control (30°C). As expected, increasing the temperature decreased the inter-electrode latency. Shorter time intervals between the initial spike (at B7) and spikes at other electrodes is evident in the leftward shift of these eAPs with increasing temperature (*A* and *B*). Temperatures are indicated by color, and eAP waveforms were peak-scaled. *B*, *top*: for each propagation signal, changes in propagation velocity were assessed by plotting the change in the latency (y) between the earliest eAP and all other eAPs of this propagation signal as a function of the latency between the initial spike and each spike time in control conditions (x). *Bottom*: the temperature-dependent increase in propagation velocity is shown as an increase in the slope of the linear fit of the data. Data from control experiments are shown on the horizontal zero line. In this example, the data were well fitted with straight lines at each temperature ($r^2 > 0.9$). *C*: for each propagation signal, we used the slope from the linear fit at each temperature to calculate the percent change in propagation velocity and the aggregate temperature data for each condition. The change as a function of temperature is well fitted with a linear function ($r^2 = 0.998$). This slope indicates that in these neurons, temperature increases the propagation velocity by ~5% per °C. Data are means ± SD. Red circle in *A* indicates the index electrode (B7) for the indicated propagation signal.

The temperature-induced changes in latency from 17 propagation signals from several different MEAs shows that this method easily resolves the effect of 2 degrees of temperature difference on action potential propagation velocity ($P < 0.005$ for each temperature comparison; Fig. 4*C*). The effect of temperature on propagation velocity is linear across a large temperature range (Chapman 1967; Franz and Iggo 1968). Fitting the mean percent change at each temperature shows that in cultured mouse hippocampal neurons, propagation velocity increased 5% for every degree increase in temperature ($r^2 = 0.98$; $m = 5.2 \pm 0.14$). These data demonstrate that the effects of manipulating propagation velocity can be quantified by sampling the effect of small latency differences at multiple sites in the axonal arbor.

Cultured mouse hippocampal neuron axons are extensive and contain multiple branches. The large two-dimensional extent of constituent propagation signal electrodes is well within the range expected from the reported length and branching patterns of hippocampal axons (Arszovszki et al. 2014; Kaech and Banker 2006). We examined the extent of axonal growth in our culture system by immunostaining cultured neurons with a marker of neuronal processes (Tuj1) and the presynaptic marker VGluT1, a marker of presynaptic terminals. To increase the chance of visualizing single axons, by minimizing contamination from processes belonging to other neurons, we decreased our plating density by 80% for these experiments. Axons were differentiated morphologically from dendrites by their caliber, longer length, and gradual taper (Kaech and Banker 2006). Figure 5 shows a neuron with an axon that bifurcates partway along its length. The meandering paths of these axonal branches span hundreds of micrometers. Branches from this axon enter regions with relatively high levels of punctate VGluT1 staining coupled with a large increase in the complexity of neuronal processes (*center left* and *bottom right*). The *inset* highlights a portion of the axon where two smaller axonal branches depart from the main branch on the left. Thus the meandering paths and extensive branching of axons in our culture system are consistent with the large and varied patterns of propagation signal electrodes in our system and show the overlap between extensive axonal processes and the two-dimensional extent of propagation signals.

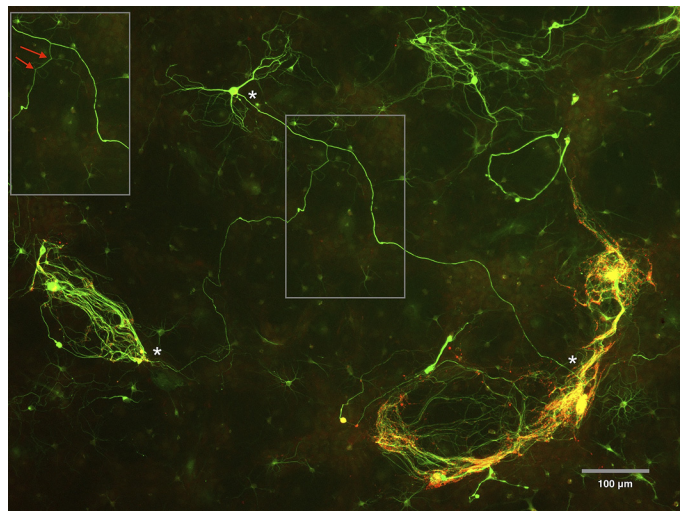

Fig. 5. Axons from cultured neurons can span hundreds of micrometers and have meandering paths and several branches. The lengths and paths displayed by axons were compared with the morphology inferred from propagation signals by immunostained hippocampal neurons with a marker expressed in axons and dendrites (Tuj1) in low-density cultures. Axons were differentiated from dendrites by their uniform caliber, longer length, and more gradual taper. The total length of the process shown between the asterisks was 1,692 μm. *Inset* highlights a portion of the axon where 2 smaller axonal branches depart from the main branch. These images confirm that neuronal processes such as axons could underlie propagation signals in our recordings.

Propagation signals are from axons. Axons have many times the density of voltage-gated sodium channels compared with dendritic or somatic membrane (Hu et al. 2009; Lorincz and Nusser 2010). Our routine detection of action potential propagation suggests that these eAPs originate from neuronal compartments with a high transmembrane conductance, such as axons. However, we cannot exclude the possibility that some of these signals result from action potential backpropagation into somatodendritic cellular regions (Spruston et al. 1995; Stuart and Sakmann 1994). The large voltage-gated sodium channel density gradient between these compartments is expected to affect the safety factor of action potential propagation (Tasaki 1953) as has been reported in these neurons (Mackenzie and Murphy 1998). Therefore, decreasing the density of active sodium channels with subsaturating concentrations of the voltage-gated sodium channel blocker TTX would collapse the propagation safety factor in dendrites to a greater extent than the axonal safety factor. We used this to examine whether propagation signals are from axons or somatodendritic regions. Neuronal sites with a low safety factor would be prone to action potential propagation failures, and thus we would expect a TTX dose-dependent change in mean eAP amplitude at these sites.

The amplitude of control eAPs (Fig. 6*A*, *left*) were not noticeably reduced by 10 nM TTX (Fig. 6*A*, *right*) in raw voltage traces from the same electrode. The electrode maps of two different propagation signals (Fig. 6*B*) indicate the electrodes at which we detected super- and subthreshold eAPs. As shown by the averaged waveforms, neither super- nor subthreshold eAPs amplitudes were attenuated by 10 nM TTX. Measurement of averaged eAPs from several propagation signals demonstrates that the mean amplitudes of super- or subthreshold eAPs were not affected by TTX (Fig. 6*C*). The $Na_V1.6$ (*Scn8a*) sodium channel subtype is highly expressed in hippocampal principal neurons (Schaller and Caldwell 2000). On the basis of the equilibrium dissociation constant estimates of 1–6 nM for these channels (Dietrich et al. 1998; Smith et al. 1998), 10 nM TTX is expected to reduce the density of active sodium channels by at least 60%. Thus reducing the density of active sodium channels by this amount had no effect on the amplitudes of propagation signal eAPs, consistent with propagation signal components originating from neuronal membrane with a high safety factor, such as axons.

A high safety factor ensures that action potentials occurring at high frequency are faithfully propagated because voltage-gated sodium channels accumulate in inactivated states at high frequencies (Goldin 2003). As shown in the example eAPs (Fig. 6*A*), subsaturating concentrations of TTX coincidentally increased the eAP firing frequency of these in vitro networks. TTX (3–10 nM) changed the spiking pattern and produced array-wide bursting. In these two cultures, the median interspike intervals (ISI) across all MEA electrodes were 211.1 and 78.6 ms before addition of TTX. These numbers decreased to 21.9 and 19.0 ms in 5 and 10 nM TTX, respectively. The burstiness index (Kumbhare and Baron 2015), a measure of spike distribution across all electrodes, was lower in the control recordings (0.456 and 0.602) than in 10 nM TTX (0.929 and 0.976), reflecting array-wide coherent bursting in the presence of TTX. In single neurons isolated as propagation signals, the average median ISI was 383.0 ± 611.2 ms in control conditions ($n = 19$). TTX application decreased the average median ISI to 27.5 ± 11.5 ms (5 nM; $n = 19$ neurons) and 35.6 ± 23.1 ms (10 nM; $n = 19$ neurons). The number of spikes in 20 nM TTX (fewer than 1% of control) was insufficient for comparative statistical analysis. The increased firing frequency caused by low concentrations of TTX increases the rigor of this test of how active sodium channel density affects the fidelity of action potential propagation. Our data show that even during action potential firing frequencies of ~30 Hz, reducing the propagation safety factor by TTX application did not reduce the mean amplitudes of super- or subthreshold eAPs (Fig. 6*C*).

Decreasing the active sodium channel density is known to decrease axonal action potential propagation velocity (Colquhoun and Ritchie 1972; Hu and Jonas 2014). As expected, TTX increased the latency between constituent propagation signal electrodes in a dose-dependent manner in our experiments (Fig. 6*D*). For example, application of TTX (10 nM) increased the latency between the index electrode (G5) and F8, compared with control (Fig. 6*D*). Lower TTX concentrations (3 and 5 nM) also significantly increased the interelectrode latency compared with control (Fig. 6, *E* and *F*). Dose-dependent changes in propagation time in these TTX concentrations were easily resolved by fitting the change in propagation time in TTX as a function of the control propagation time for each propagation signal (Fig. 6*E*). The average slope of the fit for each condition was distinct for each TTX concentration tested; the mean slopes from fits to the data were 0.01 ± 0.01 in the absence of TTX, −0.14 ± 0.02 in 3 nM ($n = 12$), −0.21 ± 0.04 in 5 nM ($n = 15$), and −0.39 ± 0.06 in 10 nM TTX ($n = 15$). These slopes reflect decreases in action potential propagation velocity of 12.2%, 17.1%, and 28.1% in 3, 5, and 10 nM TTX, respectively (Fig. 6*F*). Thus the effects of small differences in the density of active voltage-gated sodium channels are easily resolved by our methods. Moreover, when we artificially reduce the density of active voltage-gated sodium channels by more than 60%, axonal action potential propagation still occurs with high fidelity even during high-frequency firing (~30 Hz). We repeated the temperature-response curve (see Fig. 4*C*) in the presence of 6 nM TTX which should reduce the active sodium channel density by 50%. The slope of the fitted line for these experiments (4.85 ± 0.11) indicates that the temperature sensitivity of action potential propagation was unaffected by reducing the sodium channel density by 50%, assuming the TTX equilibrium dissociation constants are relatively unchanged between 30°C and 38°C. The high safety factor of these unmyelinated axons may mitigate other features affecting propagation fidelity, such as inhomogeneity in electrical capacity resulting from extensive en passant synapses and axonal branches (Lüscher and Shiner 1990a, 1990b; Mainen et al. 1995) and small caliber. That these TTX concentrations increased interelectrode latency without affecting the fidelity of action potential propagation indicates an unexpectedly high density of voltage-dependent sodium channels.

Time-dependent changes in axonal excitability. The noninvasive nature of extracellular recording is well suited to long-term monitoring of neuronal activity. We used propagation signals to monitor excitability in single axonal arbors over hours or days. For example, we monitored the propagation signal eAPs from a single neuron at all constituent electrodes during a 25-h window (Fig. 7*A*). Averaged eAP waveforms from a subset of these electrodes are shown in Fig. 7*B*. During

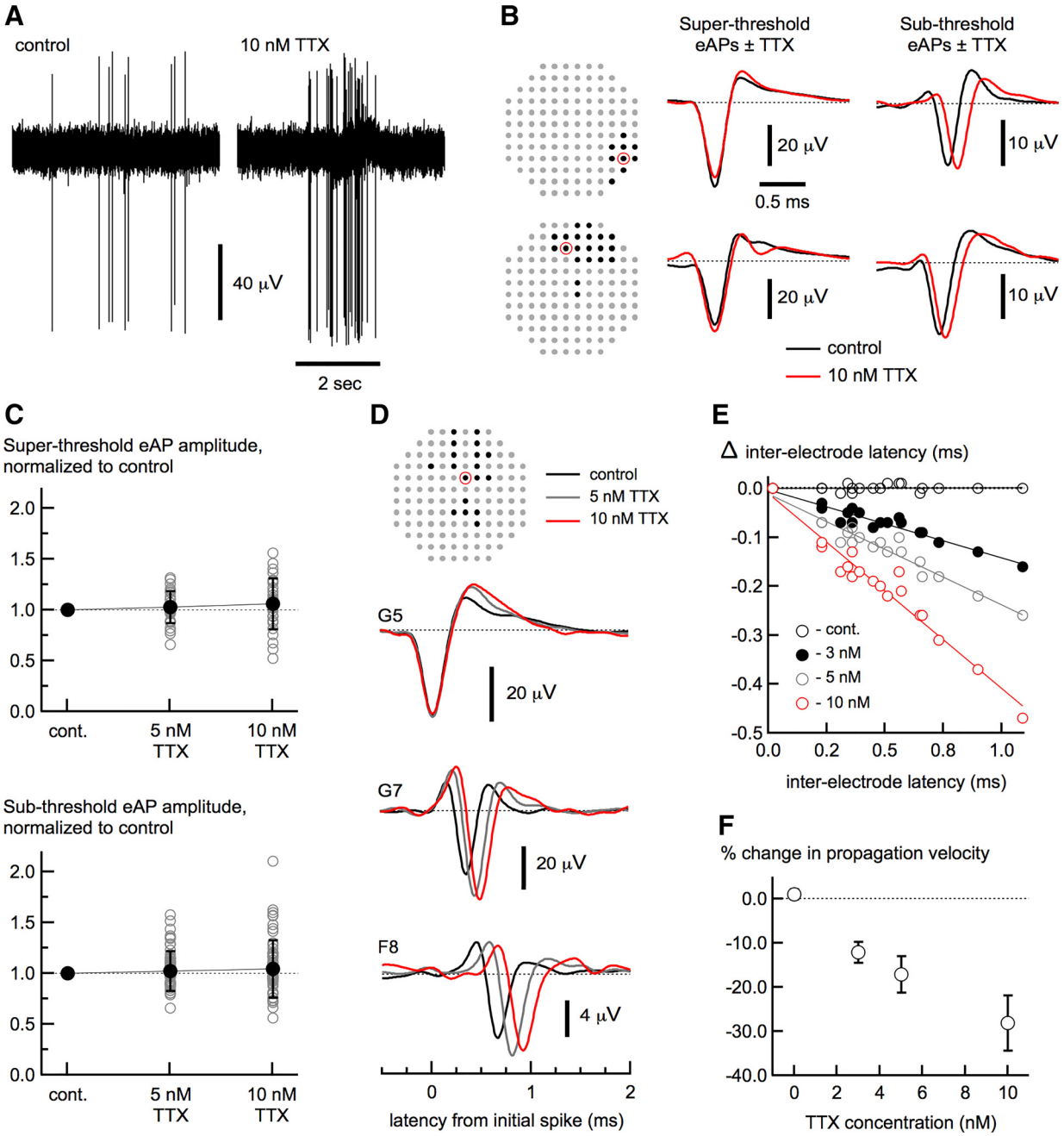

Fig. 6. Propagation signals reflect axonal action potentials. *A*: extracellular voltage traces from a single electrode are shown in control conditions (*left*) and in 10 nM TTX (*right*). *B*: signal-averaged spikes from 2 different propagation signals (array maps at *left*) are shown, with super threshold (*middle*) and subthreshold (*right*) spikes indicated. Control spikes (black traces) and spikes in TTX (red traces) are superimposed. Red circles indicate the electrodes where the earliest propagation signal extracellular action potentials (eAPs) were detected (*top*, L9; *bottom*, F3). *C*: mean amplitudes of super- (*top*) and subthreshold (*bottom*) spikes (normalized to control) from all the propagations signals in these recordings, superimposed on individual data points for these conditions. TTX (10 nM) had no effect on spike amplitude in either superthreshold spike amplitude (1.06 ± 0.25 compared with control; $n = 29$ electrodes) or subthreshold spike amplitude (1.04 ± 0.28 compared with control; $n = 67$ electrodes). These data are consistent with propagation signals predominantly representing action potential in axons. Data are from 8 propagation signals on 2 multielectrode arrays. Dashed lines are the normalized amplitude of control eAPs. *D*: in another propagation signal from these experiments, TTX decreased propagation speed, as expected from lowering the density of active voltage-gated Na^+ channels. Spikes from a subset of electrodes from this propagation signal are shown, with control spikes (black) and spikes in 5 (gray) and 10 nM TTX (red) superimposed. Traces in 3 nM TTX were excluded for clarity. In each panel, the dose-dependent increase in latency is shown as the rightward shift of the spikes with increasing TTX concentration. Red circle indicates the electrode where the initial eAPs were detected (G5). *E*: the change in latency in each condition (control, 3, 5, and 10 nM TTX) plotted as a function of the latency between the initial spike and each spike time in control conditions. Data for each condition were fitted with a linear function. *F*: the aggregate data are plotted showing the dose-dependent slowing of propagation velocity. The slope of the linear fit at each TTX concentration was used to calculate the percent change in propagation velocity. Data are means ± SD. cont., Control.

the 25-h recording interval, the eAP amplitudes at the majority of constituent electrodes from this signal remained stable (eAPs at K5 and F3, for example). However, within the same axonal arbor during the same monitoring period, we simultaneously recorded the de novo emergence of an eAP waveform at one electrode (H4) and the progressive amplitude decrease of eAPs at another electrode (E2) over the same time period. Over the course of 14 h, the resistive (negative) component of the eAP waveforms at H4 developed from the preexisting initial capacitive (positive) component, which remained otherwise unchanged (Fig. 7*B*, arrowhead). These changes were consistent with the gradual and progressive increase of active conductances of the transmembrane action potential within a previously nonexcitable portion of axon, for example. In the case of eAP elimination at the E2 electrode, the time-dependent amplitude decrease in capacitive and resistive eAP components were comparable. This observation is consistent with physical elimination, or withdrawal, of the axonal process. In contrast, a decrease in spike-coupled transmembrane current in the axon at that electrode would not be expected to affect the size of the capacitive component of the eAP waveform at this site, although other explanations, such as withdrawal of glial processes leading to decreases in apparent signal size, cannot be ruled out (Matsumura et al. 2016). Our data show that significant changes in axonal excitability can occur over several hours and imply that distinct portions of single axons can

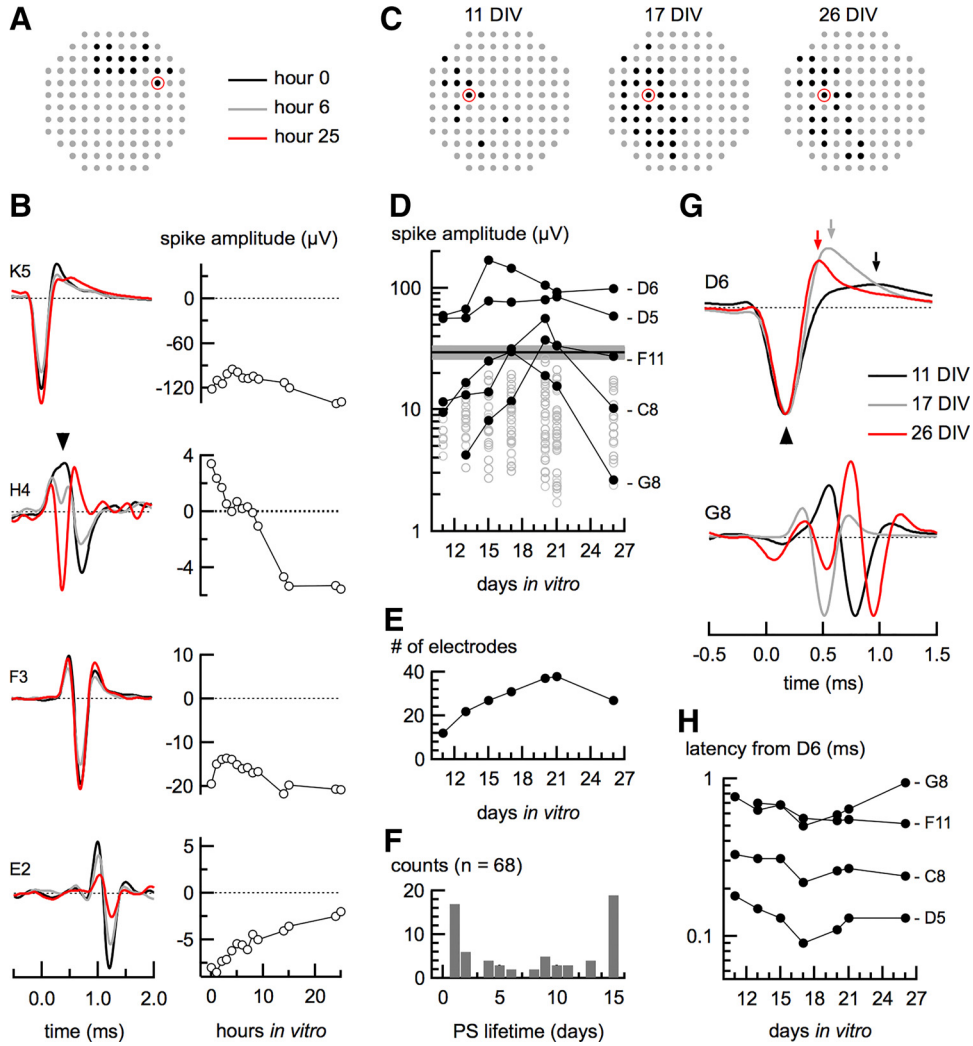

Fig. 7. Noninvasive monitoring of axonal excitability during neuronal network development. *A*: the electrode map of a propagation signal that was periodically monitored over 25 h. *B*: extracellular action potentials (eAPs) from a subset of the electrodes in *A*. During the 25-h interval, electrodes with stable eAP amplitudes (K5, F3) were measured simultaneously with the appearance of new spikes (H4; arrowhead) and the elimination of existing spikes (E2) in the same axonal arbor (*left*). Signal amplitudes for each waveform are indicated at *right*. *C*: a different propagation signal was monitored for 15 days. Maps show the constituent electrodes at each recording time (DIV, days in vitro). *D*: spike amplitudes from all contributing electrodes plotted as a function of DIV, with a subset of these highlighted (black line), indicating time-dependent changes in signal amplitude. The gray band is the mean threshold for all electrodes at 21 DIV. *E*: the total number of constituent electrodes for the propagation signal from the example in *C* and *D* at every time point. *F*: the distribution of propagation signal lifetimes (PS lifetime) plotted for 68 propagation signals from 4 multielectrode arrays monitored across 15 days. *G*, *top*: the spikes at electrode D6 are the earliest occurring for this propagation signal sequence from the example in *C* and *D* and have a waveform consistent with being at or near the site of action potential initiation. Decreases in the delays between the peak-scaled negative peak (arrowhead) and subsequent positive repolarization peaks (arrows) are consistent with a developmental decrease in spike width of the eAP at D6 between 11 and 26 DIV. A time-dependent change in the latency was also noted between eAPs at D6 and other electrodes (*G* and *H*). *G*, *bottom*: the eAP latency between electrodes D6 and G8 initially decreased before increasing to greater extent than seen in the initial measurement. *H*: changes in spike latencies were nonuniform across the axonal arbor. Red circles in *A* and *C* indicate the index electrode for the indicated propagation signal (K5 and D6, respectively).

act independently with respect to regulating excitability over this same time course.

We also used propagation signals to monitor excitability in single axons over multiple days. The electrode map in Fig. 7*C* shows constituent electrodes from one propagation signal that we monitored for 15 days. The earliest occurring spike of this signal was D6, with propagation extending outward diagonally in both directions. The electrode maps of this propagation signal at different days in vitro illustrate expansion and contraction of excitability of different portions of a single axonal arbor over time in culture. The number of constituent electrodes at which eAPs are detected in this same axonal arbor are shown over time (Fig. 7*E*). During 15 days of monitoring, we detected 68 unique propagation signals in 4 MEAs. Figure 7*F* shows the distribution of the total number of days each of these signals was detected, with many signals being detected throughout the 15-day time window (18 signals), and almost as many being detected only on a single day (17 signals). During periodic monitoring in this data set, once a propagation signal was no longer detected, we never saw instances where the same signal reappeared at a later time.

Because propagation signals are a fingerprint for the source neuron, we noninvasively recorded time-dependent changes of individual eAP waveforms at each constituent electrode within a propagation signal over a 15-day period. For this propagation signal, eAPs at D6 preceded eAPs at all other electrodes throughout the 15-day recording period (Fig. 7*C*). The time-dependent increase in spike amplitude at D6 (Fig. 7*D*), coupled with an eAP waveform lacking an initial upward capacitive peak (Fig. 7*G*), are consistent with large increases in transmembrane current at or near the AIS. The peak-to-peak interval of the spike waveform at D6 gradually shortened (Fig. 7*G*, *top*). Because the peak-to-peak interval of the extracellular eAP approximates the width at half height of the transmembrane action potential (Bean 2007), the changes in eAP waveform we report reflect a time-dependent decrease in the transmembrane action potential duration at D6. During long-term monitoring, the latency between spikes at D6 and eAPs at a subset of electrodes (C8, D5, and G8) initially showed a decrease in the interelectrode latency between *day 11* and *day 17*, followed thereafter by an increase in the latency (Fig. 7*G*, *bottom*). In contrast, the latency between spikes at D6 and F11 remained relatively stable over this time period (Fig. 7*H*). These examples illustrate that over periods of weeks, different portions of the axonal arbor from single neurons act independently from other portions, illustrating the heterogeneity of time-dependent changes in propagation speed across axonal arbor components in single neurons. Extracellular recording is used to routinely monitor neurons over long time periods. Our data illustrate how characteristics of propagation signals can be used to noninvasively monitor single neurons and single axonal arbors over several weeks.

DISCUSSION

Axons are responsible for the integration and high-fidelity transmission of neuronal input (Debanne et al. 2011). However, because of their small caliber, axons are immune from routine experimental accessibility. The data we present in this article show that MEAs with low electrode density can be used to routinely assess action potential propagation from single neurons within neuronal networks. We also have demonstrated that repeated co-occurrence of eAPs on multiple electrodes and the invariability of the timing sequence between those electrodes unambiguously confirm that these signals result from single neurons. In the context of the extracellular recording configuration, it is unprecedented to routinely and unambiguously verify that subsets of eAPs result from single identifiable neuronal sources that can be isolated from a background of eAPs from other neurons in the spike record. Averaging these signals revealed a larger cohort of electrodes with eAPs that would otherwise be below the spike detection threshold and represent the larger extent of eAPs in each axonal arbor. We used the increased range of time differences to assess the effects of manipulating propagation velocity (Figs. 4 and 6). Signal averaging eAPs revealed physiological details from different parts of the axonal membrane. The timing and the two-dimensional distribution of constituent propagation signal eAPs provides the fingerprint of each propagation signal neuron and enables us to follow individual neurons within the greater network over several days.

Techniques used to study the physiological properties of axons, such as patch clamp-based recording configurations or voltage-sensitive dyes, are technically challenging (Casale et al. 2015; Schmidt-Hieber et al. 2008). We have shown that some parallel physiological parameters can be routinely obtained from extracellular recordings with low-electrode density MEAs. Moreover, unlike recording in the patch-clamp configuration, extracellular recording is noninvasive, meaning that the spiking behavior from single neurons can be monitored for hours or days. Our results demonstrated that the development of excitability in axonal arbors proceeds gradually; expansion and retraction can occur simultaneously in different parts of the same axonal arbor (Fig. 7*B*), and thus elaboration and development of excitability in the axonal arbor is not necessarily a concerted process throughout the axon. Different branches of the axonal arbor could potentially be responding to signals associated with contraction, for example (Bishop et al. 2004). The earliest propagation signal eAP is the index around which our measurements occur because these spikes tend to be the largest and often have properties consistent with eAPs that originate from at or near the AIS. These results were surprising given that the distance between the electrodes and electrically active cellular regions is a random unknown variable and the amplitude of the extracellular voltage signal decreases steeply with distance from the source (Anastassiou et al. 2015). The detection of eAPs at or near the AIS underscores the resolving ability of this system. These features create a basis from which to explore the development of axonal excitability.

MEAs have previously been used to measure action potential propagation in axons. However, this work was done using high-electrode density arrays with thousands of electrodes (Bakkum et al. 2013; Müller et al. 2015; Radivojevic et al. 2017) or in microfluidic chambers designed to constrain axonal growth (Dworak and Wheeler 2009) and that consequently prevent interaction with other neurons. The high number of electrodes used in the former technique produces large data files that may limit the high-throughput use of this technology. The latter technique necessarily isolates axons from network interaction. Physically isolating axons in this way could mask the contribution of presynaptic conductances during action potentials and membrane inhomogeneity on action potential

propagation, for example, because axons of many hippocampal neurons have en passant presynaptic terminals along their length. Large-scale MEAs also have been used to measure action potential propagation in the retina (Li et al. 2015) in experiments that coupled electrical measurements with fluorescent labeling of small numbers of retinal ganglion cells. Combining fluorescent labeling with electrical measurement is attractive but impractical to implement in high-density neuronal cultures. Fluorescently labeling all neurons makes it difficult to follow single processes, whereas labeling a fraction of neurons may fail to routinely label neurons that underlie propagation signals. An approach combining fluorescent labeling with electrophysiological recording could be used to label single identified propagation signal neurons in our system (Pinault 1996). However, relying on changes in propagation time between component electrodes of each propagation signal for our analysis (Fig. 3) circumvents the need to know axonal path length in experiments that manipulate propagation velocity. Thus, although our methods do not give absolute values for propagation velocity, our ability to noninvasively sample from multiple sites provides the dynamic range to quantify the effects of manipulating propagation and to resolve small changes in these parameters. This creates avenues for the routine study of the physiological and pathophysiological parameters affecting action potential propagation throughout single axonal arbors.

Implications for spike-train analysis. Propagation signals were found in every recording done in mouse neuronal cultures. Our data demonstrate that when we eliminated propagation signal eAPs on all but one constituent electrode, the total number of spikes decreased by more than 40%. Propagation signals affected, on average, 25% of the electrodes in our arrays. That this form of signal redundancy has not been more commonly reported could be due to the use of larger pitch electrodes by other investigators (Shahaf and Marom 2001; Wagenaar et al. 2005), potentially decreasing the likelihood of detecting propagation signals. However, when we retrospectively doubled the electrode spacing, we did not eliminate the redundancy resulting from propagation signals.

The prevalence of propagation signals in our data records means that assessment of the significance of array-wide behavior requires their elimination. Spike sorting routines attempt to assign spikes recorded on individual electrodes into units, for the purpose of further spike-train analysis (Hill et al. 2011). Detection and elimination of propagation signals from all but one recording channel is itself a novel spike sorting step that depends only on eAP codetection at two or more electrodes. Eliminating redundant propagation signal spikes may in fact make subsequent algorithm-based spike sorting more robust. Moreover, because the constituent eAPs from each propagation signal result from single neurons, their presence in the spike train is a source of ground truth (Quiroga 2012) that can be used for testing spike sorting algorithms. We demonstrated how propagation signals could be used to test the performance of one sorting routine (Fig. 2*E*). This approach can be easily generalized to test the efficiency of other spike sorting routines as well as to test propagation signal eAPs across a range of firing frequencies (see Fig. 6*A*). Propagation signals also could be used to test sorting performance of the same signals under other different recording conditions. Our catalog of propagation signals is a resource to examine signal heterogeneity from single neurons.

Our cell culture conditions could account for why we readily observe propagation signals. In our cultures, neurons grow on a preexisting confluent glial substrate. Glia ensheathe neuronal processes during outgrowth and synaptogenesis (Theodosis et al. 2008). A confluent glial bed could create a permissive environment for growth of axons closer to MEA electrodes than they might otherwise grow. Alternatively, glia could be an electrically resistive sheet that increases eAP amplitude across all electrodes by effectively decreasing the size of the electric field (Matsumura et al. 2016). In neuronal cultures not grown on glia, we observed that neuronal processes tended to avoid the area around the electrodes, that the signal-to-noise ratio was lower than in neurons plated on a glial bed, and that propagation signals were not as notable in cultures lacking glia (data not shown). It is also possible that glia-neuron apposition increases the transmembrane current density in neurons through a glial-neuronal signaling mechanism (Fields et al. 2015; Sobieski et al. 2015; Tang et al. 2014) or by increasing the axon length and complexity of branching (Hughes et al. 2010).

Future directions. The high-throughput nature of extracellular recording with MEAs means that propagation signals can potentially be used to study channelopathies of axonal ion channels and to ask how these or other mutations affect propagation velocity. Mutations have been found in several types of voltage-gated ion channels that are typically localized to axons and are associated with phenotypes such as congenital epilepsy as well as neurodevelopmental disorders such as autism (Debanne et al. 2011; Kullmann 2010). The effects of these mutations on axonal excitability could be assessed with the approaches we have outlined in this work. Our methods could, for example, be used to study the effects of temperature on action potential propagation in models of Dravet syndrome, a condition in which patients have febrile seizures and that, in the majority of cases, is associated with mutations in the *Scn1a* subtype sodium channel (Catterall 2014). Propagation signals could be used to study other mutations in *Scn1a* that are associated with other seizure phenotypes. Patients with polymorphisms at *Scn1a* can vary in their responsiveness to commonly prescribed antiepileptic treatments (Tate et al. 2005). In human iPSC-derived neurons, propagation signals could be used to study axonal physiology within the context of human disease models. Propagation signals also could be used to understand the biophysical nature of these differences in drug sensitivity in patients with these polymorphisms.

ACKNOWLEDGMENTS

We thank Bridget N. Queenan and Carol A. Vandenburg for thoughtful reading and insightful comments on this manuscript. Data in this manuscript can be accessed from the Collaborative Research in Computational Neuroscience data sharing website (http://crcns.org/data-sets/hc/hc-15).

GRANTS

This research was sponsored by the U.S. Army Research Laboratory and Defense Advanced Research Projects Agency under Cooperative Agreement Number W911NF-15-2-0056. Additional support was also provided by the California NanoSystems Institute.

DISCLAIMERS

The views, opinions, and/or findings contained in this material are those of the authors and should not be interpreted as representing the official views or policies of the Department of Defense or the U.S. Government.

DISCLOSURES

No conflicts of interest, financial or otherwise, are declared by the authors.

AUTHOR CONTRIBUTIONS

K.R.T. conceived and designed research; K.R.T., D.C.B., C.R., M.A., and J.J. performed experiments; K.R.T. and D.C.B. analyzed data; K.R.T., D.C.B. and B.W. interpreted results of experiments; K.R.T. and M.A. prepared figures; K.R.T. drafted manuscript; K.R.T., D.C.B., and K.S.K. edited and revised manuscript; K.R.T., D.C.B., B.W., C.R., M.A., J.J., P.K.H., and K.S.K. approved final version of manuscript.

REFERENCES

Anastassiou CA, Perin R, Buzsáki G, Markram H, Koch C. Cell type- and activity-dependent extracellular correlates of intracellular spiking. *J Neurophysiol* 114: 608–623, 2015. doi:10.1152/jn.00628.2014.

Arszovszki A, Borhegyi Z, Klausberger T. Three axonal projection routes of individual pyramidal cells in the ventral CA1 hippocampus. *Front Neuroanat* 8: 53, 2014. doi:10.3389/fnana.2014.00053.

Bakkum DJ, Frey U, Radivojevic M, Russell TL, Müller J, Fiscella M, Takahashi H, Hierlemann A. Tracking axonal action potential propagation on a high-density microelectrode array across hundreds of sites. *Nat Commun* 4: 2181, 2013. doi:10.1038/ncomms3181.

Bean BP. The action potential in mammalian central neurons. *Nat Rev Neurosci* 8: 451–465, 2007. doi:10.1038/nrn2148.

Bishop DL, Misgeld T, Walsh MK, Gan WB, Lichtman JW. Axon branch removal at developing synapses by axosome shedding. *Neuron* 44: 651–661, 2004. doi:10.1016/j.neuron.2004.10.026.

Buzsáki G, Anastassiou CA, Koch C. The origin of extracellular fields and currents–EEG, ECoG, LFP and spikes. *Nat Rev Neurosci* 13: 407–420, 2012. doi:10.1038/nrn3241.

Casale AE, Foust AJ, Bal T, McCormick DA. Cortical interneuron subtypes vary in their axonal action potential properties. *J Neurosci* 35: 15555–15567, 2015. doi:10.1523/JNEUROSCI.1467-13.2015.

Catterall WA. Sodium channels, inherited epilepsy, and antiepileptic drugs. *Annu Rev Pharmacol Toxicol* 54: 317–338, 2014. doi:10.1146/annurev-pharmtox-011112-140232.

Chapman RA. Dependence on temperature of the conduction velocity of the action potential of the squid giant axon. *Nature* 213: 1143–1144, 1967. doi:10.1038/2131143a0.

Colquhoun D, Ritchie JM. The interaction at equilibrium between tetrodotoxin and mammalian non-myelinated nerve fibres. *J Physiol* 221: 533–553, 1972. doi:10.1113/jphysiol.1972.sp009766.

Cox CL, Denk W, Tank DW, Svoboda K. Action potentials reliably invade axonal arbors of rat neocortical neurons. *Proc Natl Acad Sci USA* 97: 9724–9728, 2000. doi:10.1073/pnas.170278697.

Debanne D, Campanac E, Bialowas A, Carlier E, Alcaraz G. Axon physiology. *Physiol Rev* 91: 555–602, 2011. doi:10.1152/physrev.00048.2009.

Dietrich PS, McGivern JG, Delgado SG, Koch BD, Eglen RM, Hunter JC, Sangameswaran L. Functional analysis of a voltage-gated sodium channel and its splice variant from rat dorsal root ganglia. *J Neurochem* 70: 2262–2272, 1998. doi:10.1046/j.1471-4159.1998.70062262.x.

Dworak BJ, Wheeler BC. Novel MEA platform with PDMS microtunnels enables the detection of action potential propagation from isolated axons in culture. *Lab Chip* 9: 404–410, 2009. doi:10.1039/B806689B.

Fenton AA, Muller RU. Place cell discharge is extremely variable during individual passes of the rat through the firing field. *Proc Natl Acad Sci USA* 95: 3182–3187, 1998. doi:10.1073/pnas.95.6.3182.

Fields RD, Woo DH, Basser PJ. Glial regulation of the neuronal connectome through local and long-distant communication. *Neuron* 86: 374–386, 2015. doi:10.1016/j.neuron.2015.01.014.

Franz DN, Iggo A. Conduction failure in myelinated and non-myelinated axons at low temperatures. *J Physiol* 199: 319–345, 1968. doi:10.1113/jphysiol.1968.sp008656.

Goldin AL. Mechanisms of sodium channel inactivation. *Curr Opin Neurobiol* 13: 284–290, 2003. doi:10.1016/S0959-4388(03)00065-5.

Grossman Y, Parnas I, Spira ME. Mechanisms involved in differential conduction of potentials at high frequency in a branching axon. *J Physiol* 295: 307–322, 1979. doi:10.1113/jphysiol.1979.sp012970.

Hill DN, Mehta SB, Kleinfeld D. Quality metrics to accompany spike sorting of extracellular signals. *J Neurosci* 31: 8699–8705, 2011. doi:10.1523/JNEUROSCI.0971-11.2011.

Hu H, Jonas P. A supercritical density of Na^+ channels ensures fast signaling in GABAergic interneuron axons. *Nat Neurosci* 17: 686–693, 2014. doi:10.1038/nn.3678.

Hu W, Tian C, Li T, Yang M, Hou H, Shu Y. Distinct contributions of $Na_v1.6$ and $Na_v1.2$ in action potential initiation and backpropagation. *Nat Neurosci* 12: 996–1002, 2009. doi:10.1038/nn.2359.

Hughes EG, Elmariah SB, Balice-Gordon RJ. Astrocyte secreted proteins selectively increase hippocampal GABAergic axon length, branching, and synaptogenesis. *Mol Cell Neurosci* 43: 136–145, 2010. doi:10.1016/j.mcn.2009.10.004.

Ivenshitz M, Segal M. Neuronal density determines network connectivity and spontaneous activity in cultured hippocampus. *J Neurophysiol* 104: 1052–1060, 2010. doi:10.1152/jn.00914.2009.

Kaech S, Banker G. Culturing hippocampal neurons. *Nat Protoc* 1: 2406–2415, 2006. doi:10.1038/nprot.2006.356.

Khaliq ZM, Raman IM. Axonal propagation of simple and complex spikes in cerebellar Purkinje neurons. *J Neurosci* 25: 454–463, 2005. doi:10.1523/JNEUROSCI.3045-04.2005.

Kole MHP, Ilschner SU, Kampa BM, Williams SR, Ruben PC, Stuart GJ. Action potential generation requires a high sodium channel density in the axon initial segment. *Nat Neurosci* 11: 178–186, 2008. doi:10.1038/nn2040.

Kole MHP, Stuart GJ. Signal processing in the axon initial segment. *Neuron* 73: 235–247, 2012. doi:10.1016/j.neuron.2012.01.007.

Kress GJ, Mennerick S. Action potential initiation and propagation: upstream influences on neurotransmission. *Neuroscience* 158: 211–222, 2009. doi:10.1016/j.neuroscience.2008.03.021.

Kullmann DM. Neurological channelopathies. *Annu Rev Neurosci* 33: 151–172, 2010. doi:10.1146/annurev-neuro-060909-153122.

Kumbhare D, Baron MS. A novel tri-component scheme for classifying neuronal discharge patterns. *J Neurosci Methods* 239: 148–161, 2015. doi:10.1016/j.jneumeth.2014.09.015.

Lalli MA, Jang J, Park JH, Wang Y, Guzman E, Zhou H, Audouard M, Bridges D, Tovar KR, Papuc SM, Tutulan-Cunita AC, Huang Y, Budisteanu M, Arghir A, Kosik KS. Haploinsufficiency of BAZ1B contributes to Williams syndrome through transcriptional dysregulation of neurodevelopmental pathways. *Hum Mol Genet* 25: 1294–1306, 2016. doi:10.1093/hmg/ddw010.

Lewis CM, Bosman CA, Fries P. Recording of brain activity across spatial scales. *Curr Opin Neurobiol* 32: 68–77, 2015. doi:10.1016/j.conb.2014.12.007.

Li PH, Gauthier JL, Schiff M, Sher A, Ahn D, Field GD, Greschner M, Callaway EM, Litke AM, Chichilnisky EJ. Anatomical identification of extracellularly recorded cells in large-scale multielectrode recordings. *J Neurosci* 35: 4663–4675, 2015. doi:10.1523/JNEUROSCI.3675-14.2015.

Liu MG, Chen XF, He T, Li Z, Chen J. Use of multi-electrode array recordings in studies of network synaptic plasticity in both time and space. *Neurosci Bull* 28: 409–422, 2012. doi:10.1007/s12264-012-1251-5.

Lorincz A, Nusser Z. Molecular identity of dendritic voltage-gated sodium channels. *Science* 328: 906–909, 2010. doi:10.1126/science.1187958.

Lüscher HR, Shiner JS. Computation of action potential propagation and presynaptic bouton activation in terminal arborizations of different geometries. *Biophys J* 58: 1377–1388, 1990a. doi:10.1016/S0006-3495(90)82484-X.

Lüscher HR, Shiner JS. Simulation of action potential propagation in complex terminal arborizations. *Biophys J* 58: 1389–1399, 1990b. doi:10.1016/S0006-3495(90)82485-1.

Mackenzie PJ, Murphy TH. High safety factor for action potential conduction along axons but not dendrites of cultured hippocampal and cortical neurons. *J Neurophysiol* 80: 2089–2101, 1998. doi:10.1152/jn.1998.80.4.2089.

Mainen ZF, Joerges J, Huguenard JR, Sejnowski TJ. A model of spike initiation in neocortical pyramidal neurons. *Neuron* 15: 1427–1439, 1995. doi:10.1016/0896-6273(95)90020-9.

Matsumura R, Yamamoto H, Niwano M, Hirano-Iwata A. An electrically resistive sheet of glial cells for amplifying signals of neuronal extracellular recordings. *Appl Phys Lett* 108: 023701, 2016. doi:10.1063/1.4939629.

Meeks JP, Jiang X, Mennerick S. Action potential fidelity during normal and epileptiform activity in paired soma-axon recordings from rat hippocampus. *J Physiol* 566: 425–441, 2005. doi:10.1113/jphysiol.2005.089086.

Meeks JP, Mennerick S. Action potential initiation and propagation in CA3 pyramidal axons. *J Neurophysiol* 97: 3460–3472, 2007. doi:10.1152/jn.01288.2006.

Müller J, Ballini M, Livi P, Chen Y, Radivojevic M, Shadmani A, Viswam V, Jones IL, Fiscella M, Diggelmann R, Stettler A, Frey U, Bakkum DJ, Hierlemann A. High-resolution CMOS MEA platform to study neurons at subcellular, cellular, and network levels. *Lab Chip* 15: 2767–2780, 2015. doi:10.1039/C5LC00133A.

Pinault D. A novel single-cell staining procedure performed in vivo under electrophysiological control: morpho-functional features of juxtacellularly labeled thalamic cells and other central neurons with biocytin or Neurobiotin. *J Neurosci Methods* 65: 113–136, 1996. doi:10.1016/0165-0270(95)00144-1.

Potter SM, DeMarse TB. A new approach to neural cell culture for long-term studies. *J Neurosci Methods* 110: 17–24, 2001. doi:10.1016/S0165-0270(01)00412-5.

Prentice JS, Homann J, Simmons KD, Tkačik G, Balasubramanian V, Nelson PC. Fast, scalable, Bayesian spike identification for multi-electrode arrays. *PLoS One* 6: e19884, 2011. doi:10.1371/journal.pone.0019884.

Quiroga RQ. Spike sorting. *Curr Biol* 22: R45–R46, 2012. doi:10.1016/j.cub.2011.11.005.

Quiroga RQ, Nadasdy Z, Ben-Shaul Y. Unsupervised spike detection and sorting with wavelets and superparamagnetic clustering. *Neural Comput* 16: 1661–1687, 2004. doi:10.1162/089976604774201631.

Raastad M, Shepherd GM. Single-axon action potentials in the rat hippocampal cortex. *J Physiol* 548: 745–752, 2003. doi:10.1113/jphysiol.2002.032706.

Radivojevic M, Franke F, Altermatt M, Müller J, Hierlemann A, Bakkum DJ. Tracking individual action potentials throughout mammalian axonal arbors. *eLife* 6: e30198, 2017. doi:10.7554/eLife.30198.

Ranck JB Jr. Studies on single neurons in dorsal hippocampal formation and septum in unrestrained rats. I. Behavioral correlates and firing repertoires. *Exp Neurol* 41: 462–531, 1973. doi:10.1016/0014-4886(73)90290-2.

Schaller KL, Caldwell JH. Developmental and regional expression of sodium channel isoform NaCh6 in the rat central nervous system. *J Comp Neurol* 420: 84–97, 2000. doi:10.1002/(SICI)1096-9861(20000424)420:1<84::AID-CNE6>3.0.CO;2-9.

Schmidt-Hieber C, Jonas P, Bischofberger J. Action potential initiation and propagation in hippocampal mossy fibre axons. *J Physiol* 586: 1849–1857, 2008. doi:10.1113/jphysiol.2007.150151.

Shahaf G, Marom S. Learning in networks of cortical neurons. *J Neurosci* 21: 8782–8788, 2001. doi:10.1523/JNEUROSCI.21-22-08782.2001.

Smith MR, Smith RD, Plummer NW, Meisler MH, Goldin AL. Functional analysis of the mouse Scn8a sodium channel. *J Neurosci* 18: 6093–6102, 1998. doi:10.1523/JNEUROSCI.18-16-06093.1998.

Sobieski C, Jiang X, Crawford DC, Mennerick S. Loss of local astrocyte support disrupts action potential propagation and glutamate release synchrony from unmyelinated hippocampal axon terminals in vitro. *J Neurosci* 35: 11105–11117, 2015. doi:10.1523/JNEUROSCI.1289-15.2015.

Soleng AF, Baginskas A, Andersen P, Raastad M. Activity-dependent excitability changes in hippocampal CA3 cell Schaffer axons. *J Physiol* 560: 491–503, 2004. doi:10.1113/jphysiol.2004.071225.

Spruston N, Schiller Y, Stuart G, Sakmann B. Activity-dependent action potential invasion and calcium influx into hippocampal CA1 dendrites. *Science* 268: 297–300, 1995. doi:10.1126/science.7716524.

Stuart GJ, Sakmann B. Active propagation of somatic action potentials into neocortical pyramidal cell dendrites. *Nature* 367: 69–72, 1994. doi:10.1038/367069a0.

Tang F, Lane S, Korsak A, Paton JF, Gourine AV, Kasparov S, Teschemacher AG. Lactate-mediated glia-neuronal signalling in the mammalian brain. *Nat Commun* 5: 3284, 2014. [Erratum in *Nat Commun* 5: 3993, 2014.] doi:10.1038/ncomms4284.

Tasaki I. *Nervous Transmission*. Springfield, IL: Charles C. Thomas, 1953.

Tate SK, Depondt C, Sisodiya SM, Cavalleri GL, Schorge S, Soranzo N, Thom M, Sen A, Shorvon SD, Sander JW, Wood NW, Goldstein DB. Genetic predictors of the maximum doses patients receive during clinical use of the anti-epileptic drugs carbamazepine and phenytoin. *Proc Natl Acad Sci USA* 102: 5507–5512, 2005. doi:10.1073/pnas.0407346102.

Theodosis DT, Poulain DA, Oliet SHR. Activity-dependent structural and functional plasticity of astrocyte-neuron interactions. *Physiol Rev* 88: 983–1008, 2008. doi:10.1152/physrev.00036.2007.

Tovar KR, Westbrook GL. Amino-terminal ligands prolong NMDA receptor-mediated EPSCs. *J Neurosci* 32: 8065–8073, 2012. doi:10.1523/JNEUROSCI.0538-12.2012.

Wagenaar DA, Madhavan R, Pine J, Potter SM. Controlling bursting in cortical cultures with closed-loop multi-electrode stimulation. *J Neurosci* 25: 680–688, 2005. doi:10.1523/JNEUROSCI.4209-04.2005.

Westerfield M, Joyner RW, Moore JW. Temperature-sensitive conduction failure at axon branch points. *J Neurophysiol* 41: 1–8, 1978. doi:10.1152/jn.1978.41.1.1.

Zhou WL, Yan P, Wuskell JP, Loew LM, Antic SD. Intracellular long-wavelength voltage-sensitive dyes for studying the dynamics of action potentials in axons and thin dendrites. *J Neurosci Methods* 164: 225–239, 2007. doi:10.1016/j.jneumeth.2007.05.002.